Published in final edited form as:
Nature. 2015 June 25; 522(7557): 450–454. doi:10.1038/nature14471.

Atomic structure of the APC/C and its mechanism of protein ubiquitination

Leifu Chang[#], **Ziguo Zhang**[#], **Jing Yang**, **Stephen H. McLaughlin**, and **David Barford**
MRC Laboratory of Molecular Biology, Francis Crick Avenue, Cambridge, CB2 0QH, UK

[#] These authors contributed equally to this work.

Abstract

The anaphase-promoting complex (APC/C) is a multimeric RING E3 ubiquitin ligase that controls chromosome segregation and mitotic exit. Its regulation by coactivator subunits, phosphorylation, the mitotic checkpoint complex, and interphase inhibitor Emi1 ensures the correct order and timing of distinct cell cycle transitions. Here, we used cryo-electron microscopy to determine atomic structures of APC/C-coactivator complexes with either Emi1 or a UbcH10-ubiquitin conjugate. These structures define the architecture of all APC/C subunits, the position of the catalytic module, and explain how Emi1 mediates inhibition of the two E2s UbcH10 and Ube2S. Definition of Cdh1 interactions with the APC/C indicates how they are antagonized by Cdh1 phosphorylation. The structure of the APC/C with UbcH10-ubiquitin reveals insights into the initiating ubiquitination reaction. Our results provide a quantitative framework for the design of experiments to further investigate APC/C functions *in vivo*.

The activities of the diverse proteins that orchestrate the sequential biochemical and morphological changes intrinsic to the cell division cycle are controlled through the integration of protein phosphorylation, proteolysis and changes in gene expression. Two cullin-RING E3 ubiquitin ligases, the APC/C and SCF, catalyze the ubiquitination of multiple cell cycle proteins to regulate their proteasome-mediated proteolysis. By regulating the ordered degradation of substrates such as cyclins, securin, mitotic kinases, and microtubule motors and assembly factors, the APC/C controls sister chromatid segregation, cytokinesis and the initiation of chromosome duplication [1-3].

The APC/C is a large assembly comprising 19 subunits [4]. Its activity depends on the association of one of two coactivator subunits (either Cdc20 or Cdh1) that specify substrate recognition and stimulate the catalytic activity of APC/C – E2 complexes [4-7]. Coactivators engage the APC/C through a conserved N-terminal C box motif and a C-terminal Ile-Arg

Correspondence should be addressed to D.B. (dbarford@mrc-lmb.cam.ac.uk).
Author contributions. L.C. prepared grids, collected and analyzed EM data and determined the 3D reconstructions, fitted coordinates and built models, prepared figures, co-wrote the paper. Z.Z. designed and made constructs, performed biochemical analysis and purified proteins. J.Y. prepared and purified the complexes and performed biochemical analysis. S.H.McL. performed and analyzed SPR experiments. D.B. directed the project, built models and co-wrote the paper.

Author information. EM maps are deposited with the EM-DB with accession codes: 2924 (APC/$C^{Cdh1.Emi1}$), 2925 (APC/$C^{Cdh1.Hsl1.UbcH10-Ub}$), 2926 (APC/$C^{Cdh1.Hsl1.Apc11-UbcH10}$). APC/$C^{Cdh1.Emi1}$ coords have accession code 4ui9.

The authors declare no competing financial interests.

Europe PMC Funders Author Manuscripts

(IR) tail [2,3]. Cyclin-dependent kinase (CDK) phosphorylates the APC/C promoting Cdc20 association [8,9]. In contrast, Cdh1 is negatively regulated by phosphorylation [8,10,11].

APC/C activity is repressed by the spindle assembly checkpoint (SAC) to ensure accurate sister chromosome segregation [3]. The SAC effector, the mitotic checkpoint complex (MCC), inhibits mitotic APC/C^{Cdc20} whereas Emi1 (early mitotic inhibitor1) inhibits APC/C^{Cdh1} during interphase [12]. Similar to the MCC, Emi1 blocks D box recognition by APC/C-coactivator complexes. However, Emi1 also antagonizes the two E2s, UbcH10 and Ube2S, that pair with the APC/C and which are responsible for catalyzing ubiquitin chain initiation and elongation, respectively [13-17].

A quantitative mechanistic understanding of the APC/C requires structural information to atomic resolution. We previously described the human APC/C^{Cdh1}-substrate complex (APC/$C^{Cdh1.Hsl1}$) from a cryo-EM reconstruction allowing definition of the overall architecture of the multi-subunit assembly [4]. Still, the atomic structures of several large and most small APC/C subunits, and the regulatory N-terminal domain (NTD) of Cdh1 were unknown, which together with the flexibility of the catalytic module comprising the RING subunit Apc11 and the C-terminal domain of Apc2 (Apc2^{CTD}) limited our understanding of the complex.

Here, we used recombinant APC/C^{Cdh1} in complex with Emi1 (APC/$C^{Cdh1.Emi1}$) to determine an atomic model of the APC/C to 3.6 Å resolution (Extended Data Figs 1 and 2 and Extended Data Table 1). This structure, together with an APC/C^{Cdh1} – UbcH10 complex, reveals details of the initiating ubiquitination reaction and how Emi1 inhibits UbcH10 and Ube2S [13,14].

Atomic structure of APC/$C^{Cdh1.Emi1}$

Figs 1a, b show two views of the atomic model of APC/$C^{Cdh1.Emi1}$ (Supplementary Video 1). A local resolution map indicates that most of the static regions of the complex are at ~3.2 Å resolution (Extended Data Fig. 1). Specific regions of the molecule, including the catalytic module and the Cdh1^{WD40} domain are more mobile and visualized at lower resolution (Extended Data Fig. 1).

Similar to APC/$C^{Cdh1.Hsl1}$ (Ref. [4]), 60% of molecules are the coactivator-bound APC/$C^{Cdh1.Emi1}$ complex, with the remainder in the apo state. APC/$C^{Cdh1.Emi1}$ adopts the active conformation with the platform sub-domain, incorporating Apc2^{CTD}-Apc11, in the upward position (Fig. 1a). However, in contrast with APC/$C^{Cdh1.Hsl1}$ where Apc2^{CTD}-Apc11 is flexible [4], Emi1 stabilizes Apc2^{CTD}-Apc11 by bridging it to Apc1 (Fig. 1a).

With the APC/$C^{Cdh1.Emi1}$ EM map at 3.6 Å resolution we built a complete atomic model of the complex. Existing crystal structures, complemented by newly determined structures of Apc4 and the N-terminal domain of Apc5 (unpublished data), together with homology models (Extended Data Tables 2 & 3), were used to guide building of most large APC/C subunits. For Apc1, fitting to the N-terminal Apc1^{WD40} domain and the densities N- and C-terminal to its central PC domain (Apc1^{PC}) were performed *ab initio*. These two regions coalesce to form Apc1^{Mid} that connects Apc1^{WD40} with Apc1^{PC} and comprises an α-

solenoid capped by a β-sandwich (Extended Data Fig. 3a). Apc13 and Apc16 of the TPR lobe interact with structurally homologous symmetry-related sites on the four TPR homo-dimers (Extended Data Figs 3b, c). The refined APC/C$^{Cdh1.Emi1}$ model has excellent stereochemistry and is in good agreement with the EM density map (Extended Data Fig. 2 and Extended Data Table 1).

Cdh1^{NTD} binds to Apc1 and Apc8

In the APC/C$^{Cdh1.Emi1}$ EM map, the Cdh1^{NTD}-assigned region shows clearly resolved side chain features (Extended Data Fig. 1g). Four distinct segments of Cdh1^{NTD} are organized into two mini-domains (Fig. 2a). Segments 1 and 3 interact with Apc8B, whereas segments 2 and 4 interact with Apc1^{PC}. Segment 1 incorporates the seven-residue C box (residues 46-52) (Extended Data Fig. 3d), which through extensive contacts with Apc8 is a key determinate of Cdh1^{NTD} – APC/C interactions. The C box adopts a hairpin conformation that inserts into the TPR superhelix of Apc8 (Figs 2a, b). Asp46, Arg47 and Arg52 of the C box form a network of electrostatic interactions, whereas Phe48 and Ile49 mediate non-polar contacts. Strikingly, Arg47 and Ile49 bind a site on Apc8 that is structurally homologous to the IR tail-binding site of Apc3, a paralog of Apc8 (Figs 2b-d). In both TPR proteins, three invariant residues (Asn339, Ser342 and Glu374 of Apc8) coordinate the Arg guanidinium group, with the Arg's aliphatic moiety sandwiched between a conserved aromatic residue and an invariant Leu (Figs 2b-d). The aliphatic side chain of the C box-Ile49 is flanked by two tyrosines (both conserved in Apc3) and a Met (Leu in Apc3). Segment 3's main role is to stabilize the conformation of segment 1 by contributing Leu127 and Phe128 to a cluster of hydrophobic residues at the Apc8 – Cdh1^{NTD} interface (Fig. 2a). Mutation of both residues severely abrogates Cdh1 activity (Fig. 2e **[lanes 1 and 4]**).

Segment 2 forms a leucine zipper-like α-helical interface with two outer α-helices of Apc1^{PC}, an interaction mediated by three conserved leucines (Fig. 2a). The α-helix of segment 4 aligns antiparallel to segment 2 (Fig. 2a). It includes the KLLR sequence (Extended Data Fig. 3d), structurally similar to the KILR motif of Cdc20^{NTD} that interacts with Mad2 as a β-strand [18], and is implicated in mediating APC/C – Cdc20 interactions [19]. Leu160 and Leu161 of the KLLR sequence, together with Val153 of segment 4, contribute to the hydrophobic interface of segment 2 and Apc1^{PC} (Figs 2a, f).

The C-terminal ten residues of Cdh1 form the IR tail. This is well ordered and adopts a mainly α-helical conformation that inserts into the TPR superhelix of Apc3A (Fig. 2c and Extended Data Fig. 3b). The universally invariant C-terminal Arg496 contacts residues of Apc3A analogous to how Arg47 of the C box contacts Apc8 (Figs 2b, c). The adjacent Ile of the IR tail packs into a hydrophobic pocket on Apc3. Through its C-terminal IR residues, Apc10 interacts with a similar conformation to the symmetry-related IR tail-binding site on the Apc3 homo-dimer (Apc3B) (Fig. 2d).

Both C box-Arg47 and its coordinating Asn339 residue (Fig. 2b) are required for coactivator binding to the APC/C [20-22], and the biochemically defined interaction of Cdc20^{NTD}. Disruption of Apc3 residues Asn575 and Leu606 impaired coactivator binding [21]. Furthermore, temperature-sensitive cell cycle mutations of *S. cerevisiae CDC23* (Apc8)

(Ref. [23]) can be rationalized due to their disruption of the C box-receptor (Fig. 2b). In support of these previous data, mutating Asn339 and Glu374 of Apc8 that engage Arg47 abolished the capacity of Cdh1 to activate the APC/C (Fig. 2e). By contrast, mutation of the structurally related-Arg493 of the IR tail only reduced APC/C^{Cdh1} activity (Extended Data Fig. 4a). Arg52 of the C box forms a salt bridge with Glu410 of Apc8 (Fig. 2b), and disrupting either residue eliminates APC/C activity (Fig. 2e).

To explore the basis for the negative regulation of coactivators by CDK phosphorylation [8,10,11], we first identified which of the nine potential CDK phosphorylation sites in $Cdh1^{NTD}$ account for this control. Four of these sites (S40, T121, S151, S163) (Extended Data Fig. 3d) are both necessary and sufficient to mediate CDK-regulation of Cdh1 (Fig. 2g, **lanes 1-6**), in agreement with [24]. Although S40, S151 and S163 (but not T121) phosphorylation each contributes individually to a degree of Cdh1 inactivation (Fig. 2g, **lanes 7-14**), simultaneous phosphorylation of all sites was required to inactivate Cdh1 completely (Fig. 2g, **lanes 1-4**). Phosphorylation of these sites would destabilize $Cdh1^{NTD}$ – APC/C interactions through electrostatic repulsion and steric clashes (Fig. 2a). Ser40 is immediately N-terminal to the C box, whereas the side chains of Ser151 and Ser163 flank the KLLR sequence of segment 4 and contact $Apc1^{PC}$ (Fig. 2a).

Emi1 inhibits UbcH10 and Ube2S binding

Four functional elements of Emi1 mediate APC/C^{Cdh1} inhibition [13,14,25]. A D box motif that occludes substrate recognition is connected through a linker to a zinc-binding region (ZBR) ($Emi1^{ZBR}$) that interferes with UbcH10-dependent APC/C activity [13,14,25]. A C-terminal LRRL sequence (LR tail: $Emi1^{LR}$), identical to the LRRL motif required for Ube2S association with the APC/C [4,7,14], antagonizes Ube2S [13,14]. In the APC/$C^{Cdh1.Emi1}$ structure we identified EM density corresponding to all four elements (Figs 3a, b). This agrees with a previous EM study at lower resolution that had assigned Emi1 density bridging the substrate recognition module and platform [13]. In our structure, the Emi1-D box is engaged by the D box co-receptor of Cdh1 and Apc10 (Figs 1a and 3a). We identified EM density matching the In-Between-RING (IBR) architecture of $Emi1^{ZBR}$ (Ref. [13]) associated with $Apc2^{CTD}$-Apc11 (Figs 3a, b). The domain connects these subunits to an insertion within $Apc1^{PC}$. In the EM map, part of the $Emi1^{Linker}$ forms an α-helix that packs against the $Emi1^{ZBR}$ β-sheet and docks onto the UbcH10-binding site of $Apc11^{RING}$ (Figs 3a, b). This blocks UbcH10 association with $Apc11^{RING}$.

We assigned $Emi1^{LR}$ as a helical density feature to a site on $Apc2^{CTD}$ at the interface of its four-helix bundle and α/β sub-domain, adjacent to $Apc4^{WD40}$ (Fig. 3b & Extended Data Fig. 2f), and in agreement with biochemical studies [14,26]. $Emi1^{ZBR}$ does not contribute to inhibiting Ube2S-catalyzed ubiquitination reactions [13,14], and our structure shows that Ube2S-specific sites on $Apc11^{RING}$ (Ref. [26]) are not blocked by $Emi1^{ZBR}$ (Fig. 3b).

The $Apc11^{RING}$-assigned density of APC/$C^{Cdh1.Emi1}$ was a perfect match to the crystal structure of $Apc11^{RING}$ (Ref. [26]) (Figs 3a, b and Extended Data Figs 5a). Assignment of EM density to $Apc2^{CTD}$-Apc11 indicated disorder of the $Apc2^{CTD}$ WHB sub-domain. The

juxtaposition of Apc11^{RING} and Apc2^{CTD} is similar to the swung out conformation of Rbx1^{RING} in activated Cul5-Rbx1 (Ref. [27]) (Extended Data Figs 5b-e).

Apc11^{RING} positions UbcH10-ubiquitin

Apc11^{RING} stimulates ubiquitination reactions catalyzed by the initiating E2s – UbcH10 and UbcH5, and the elongating E2 – Ube2S [26]. Activation of UbcH10 involves a canonical interaction between its UBC domain and Apc11^{RING} (Ref. [26]), whereas for Ube2S, Apc11^{RING} is repurposed to position the acceptor ubiquitin for modification by the Ube2S-ubiquitin conjugate [26]. To understand substrate ubiquitination catalyzed by the APC/C – UbcH10 pair, we determined a 3D reconstruction of an APC/C^{Cdh1}-substrate complex (APC/C$^{Cdh1.Hsl1}$) with a UbcH10-ubiquitin conjugate. Because of the low affinity of APC/C – UbcH10-ubiquitin interactions [4], to facilitate generation of APC/C$^{Cdh1.Hsl1.UbcH10\text{-}Ub}$ complexes suitable for cryo-EM, we fused the LR tail of Ube2S to the C-terminus of UbcH10 (UbcH10^{LR}) (Extended Data Fig. 1c). This approach is similar to that used to target the heterologous E2 Ube2G2 to the APC/C [28]. The UbcH10^{LR} fusion protein exhibited a 100-fold slower dissociation rate and a 10-fold higher affinity for the APC/C (Extended Data Table 3). Competition and mutagenesis analyses indicated that the UBC domain of UbcH10^{LR} binds the physiological site on the APC/C (Extended Data Figs 4b, c). Ubiquitination assays showed that UbcH10^{LR} and UbcH10 had indistinguishable activity (Extended Data Fig. 4d).

The APC/C$^{Cdh1.Hsl1.UbcH10\text{-}Ub}$ complex was determined to 4.1 Å resolution (Extended Data Fig. 2c & Extended Table 1b). Similar to APC/C$^{Cdh1.Emi1}$, 3D classification revealed both ternary (coactivator-bound) and apo states (Extended Data Fig. 6a **– cycle 1**). Visible EM density for the LR tail in the ternary state indicated stoichiometric association of UbcH10-Ub (Extended Data Fig. 2f). However, density corresponding to UbcH10, connected to Apc2^{CTD}-Apc11^{RING}, was weak.

Extensive 3D classification of APC/C$^{Cdh1.Hsl1.UbcH10\text{-}Ub}$ revealed structural variability of the UbcH10 density consistent with low occupancy of the UBC domain (~36%), coupled with minor conformational variability of the Apc2^{CTD}-Apc11-UbcH10 catalytic module (Extended Data Fig. 6a **– cycle 2**). Subjecting a major 3D class for further classification generated a 3D class with clearly resolved UbcH10 density (Extended Data Fig. 6a **– cycle 3 – class 5** and Extended Data Figs 6b, c). This structural class was suitable for docking UbcH10 coordinates (Figs 4a, b) and is representative of other APC/C-UbcH10 conformational states (Extended Data Figs 6d, e). Relative to APC/C$^{Cdh1.Emi1}$, Apc2^{CTD}-Apc11^{RING} tilts slightly at the Apc2^{NTD}-Apc2^{CTD} interface (Extended Data Fig. 5f), and Apc11^{RING} tilts relative to Apc2^{CTD} (Fig. 4c). UbcH10 and Apc11^{RING} interact through a canonical E2-RING mechanism [26], thus docking of UbcH10 – Apc11^{RING} was guided by crystal structures of RING-UbcH5-ubiquitin complexes [29,30] (Figs 4a, b). Importantly, this showed that density for ubiquitin was not visible in the EM map, indicating that the ubiquitin moiety is flexible (Figs 4a, b and Fig. 5a). Consistent with this conclusion, a reconstruction of an APC/C$^{Cdh1.Hsl1.Apc11\text{-}UbcH10}$ fusion complex (Extended Data Figs 1b & 2d & Extended Table 1b), and a negative stain structure of APC/C$^{Cdh1.Hsl1}$ with a huge

excess of UbcH10, showed that the shape of the UbcH10-assigned density resembled the UbcH10-Ub density in the APC/C$^{Cdh1.Hsl1.UbcH10\text{-}Ub}$ map (Extended Data Figs 6c & 7).

Since UbcH10 and Apc11^{RING} interact through a canonical E2-RING interface (Figs 4a, b), the APC/C likely stimulates the intrinsic catalytic activity of UbcH10-ubiquitin [31] by promoting a closed conformation that primes the UbcH10-ubiquitin thioester bond [15,29,30,32-36]. In agreement with this, mutation of Ile36 that contacts Apc11^{RING} (Refs [29,30,34]) and Ile44 that contacts UbcH10 (Refs [15,29,30,32,34]) (Fig. 5a) ablates APC/C-catalyzed ubiquitination (Extended Data Figs 4e, f). Nevertheless, the absence of EM density for the ubiquitin moiety of the UbcH10^{LR}-ubiquitin conjugate indicates that APC/C does not stabilize a static closed UbcH10-ubiquitin conformation [29,30,34]. Modelling shows that only Apc11^{RING} would interact with ubiquitin in the closed UbcH10-ubiquitin conformation (Fig. 5a), whereas in crystal structures of RING–UbcH5-ubiquitin conjugates where ubiquitin is static, either a second RING subunit [29,30] or a non-RING element [34] also contact ubiquitin to enhance catalytic efficiency. The APC/C is reminiscent of other single domain RING and U box E3s that bias the E2-ubiquitin conformation from multiple extended states to the closed state [33,37]. An interesting possibility is that substrate initiation motifs that promote lysine ubiquitination [38] may induce a closed UbcH10-ubiquitin conformation.

Defining target lysine ubiquitination

The APC/C$^{Cdh1.Hsl1.UbcH10\text{-}Ub}$ model shows that the UbcH10 catalytic Cys is some 40 Å from the C-terminus of a D box at the D box receptor [39] (Fig. 5a). An extended linker of ten residues would place a lysine C-terminal to the D box at the UbcH10-Ub catalytic site (Fig. 5a). Consistent with this, peptides with a lysine at positions K10, K13 and K18 relative to the D box were ubiquitinated, but not peptides with lysines at K1, K4 and K7 (Figs 5b, c). Peptides modelled on known APC/C substrates: geminin (Lys50, equivalent to K18, [Ref. [38]]) and cyclin B (Lys64, equivalent to K13) were also ubiquitinated.

Conclusions

The atomic structure of the APC/C provides a quantitative framework for understanding APC/C mechanisms and the basis for future studies to investigate mechanisms of control by phosphorylation and the MCC. We speculate that in the APC/C^{Cdc20} complex inhibited by MCC, the second C box-receptor of the Apc8 homo-dimer may bind the Cdc20 subunit of the MCC [3,40]. TAME is an Ile-Arg dipeptide APC/C inhibitor [41]. Its proposed mechanism is to inhibit coactivator association by competing for the IR tail-binding site on Apc3. The homology of the C box-receptor of Apc8 and the IR tail-receptor of Apc3 suggests that TAME may also disrupt C box – APC/C interactions, a notion consistent with the more important role of the C box for APC/C activity and cell viability [20].

Methods

Cloning, expression and purification of recombinant human APC/C

The genes for recombinant human APC/C$^{Cdh1.Emi1}$ were cloned into a modified MultiBac system as described previously [42]. Two pU2 plasmids were prepared: pU2-1 harbouring genes for Apc1 and Apc11, and pU2-2 containing genes for Apc5, Apc8, Apc10, Apc13 and Apc15. Two pF2 plasmids were prepared: pF2-1 harbouring genes for Apc3, Apc6, Apc7, Apc12 and Apc16, and pF2-2 containing genes for Apc2, Apc4, Cdh1 and Emi1. A C-terminal *tev* cleavable double Strep-II tag was added to Apc4 for purification of the complex. Two bacmids were prepared from these four plasmids, resulting in two viruses harbouring all 16 genes with each gene flanked by its own promoter and terminator. The APC/C$^{Cdh1.Emi1}$ ternary complex was co-expressed from these two viruses in High 5 insect cells. The complex was purified by a combination of Strep-Tactin (Qiagen), anion exchange chromatography Mono Q and Superose 6 size-exclusion chromatography (GE Healthcare) similar to [42].

APC/C$^{Cdh1.Hsl1.Apc11\text{-}UbcH10}$ was cloned, expressed and purified as described previously [4], except that Apc11 was replaced with Apc11 fused to UbcH10$^{(C114K)}$ at its C-terminus by a 30-residue linker of GSA repeats. A similar version of APC/C$^{Cdh1.Hsl1.Apc11\text{-}UbcH10}$ fusion complex was also prepared using wild type UbcH10 instead of UbcH10$^{(C114K)}$ for activity studies.

UbcH10^{LR} was constructed by fusion of residues 154-222 of Ube2S to the C-terminus of UbcH10$^{(C114K)}$ in the pET28 plasmid. An N-terminal His_6-tev site was added to UbcH10^{LR}. In the purified ubiquitin and UbcH10^{LR} proteins the His_6 tag was retained on ubiquitin, but cleaved from UbcH10^{LR}. The UbcH10^{LR}-Ub conjugate was generated as previously described [4] with minor modifications. UbcH10^{LR} (200 μM) was incubated with His_6-tagged ubiquitin (400 μM) at 25 °C for 16 h in a buffer containing 5 μM UBA1, 3 mM ATP, 5 mM $MgCl_2$, 0.8 mM TCEP, 150 mM NaCl, 50 mM Tris.HCl (pH 10.0). Additional 2 mM ATP and 2 μM UBA1 were added to the reaction and incubated at 25 °C for another 8 h. The UbcH10^{LR}-Ub conjugate was separated from unconjugated UbcH10^{LR} by Ni-NTA and separated from free ubiquitin by S75 size-exclusion chromatography (GE Healthcare). APC/C$^{Cdh1.Hsl1}$ was purified as described previously [4]. The purified APC/C$^{Cdh1.Hsl1}$ was concentrated to 3 μM. APC/C$^{Cdh1.Hsl1.UbcH10\text{-}Ub}$ was reconstituted by incubating APC/C$^{Cdh1.Hsl1}$ with UbcH10^{LR}-Ub conjugate in a 1:3 molar ratio on ice for 30 min in buffer of 20 mM HEPES (pH 8.0), 150 mM NaCl, 1 mM DTT. Just prior to applying to EM grids, the sample was cross-linked with glutaraldehyde (GA) by adding 0.03% GA, and incubated on ice for 40 min. The reaction was quenched by adding 40 mM Tris.HCl (pH 8.0). The quenched sample was incubated on ice for 30 min before further purification with size-exclusion Superose 6. A similar UbcH10^{LR} protein was made by using wild type UbcH10 for use in activity tests. Surface plasmon resonance experiments for UbcH10^{LR} and APC/C were performed as described previously [4]. The Y91A and S123G mutants of UbcH10 and UbcH10LR were prepared as for wild type UbcH10.

For ubiquitination reactions, APC/C and its variants with mutant subunits (Apc1 and Apc8) were cloned, expressed and purified as for apo APC/C [42] by replacing the target subunit

with its mutant. These include APC/C with Apc1$^{L1197A/L1227A/I1230A/H1231A}$, APC/C with Apc8$^{N339A/E374A}$, APC/C with Apc8$^{N339A/E374R}$, APC/C with Apc8^{E410R}.

Human Cdh1 was cloned into pU1 with an N-terminal His_6 followed by an HA tag. Based on this plasmid, variants of Cdh1 mutations were made. These were Cdh1$^{L160A/L161A}$, Cdh1$^{Y91A/L99A}$, Cdh1$^{L127A/F128A}$, Cdh1$^{L94A/L95A/V153A}$, Cdh1$^{L160A/L161AY91A/L99A}$, Cdh1 $^{L160A/L161A/L127A/F128A}$, Cdh1$^{Y91A/L99A/L127A/F128A}$, Cdh1$^{L160A/L161A/Y91A/L99A/L127A/F128A}$, Cdh1^{R47A}, Cdh1^{R52A}, Cdh1^{R493A}, Cdh1$^{T121A/S151A/S163A}$, Cdh1$^{S40A/S151A/S163A}$, Cdh1$^{S40A/T121A/S163A}$, Cdh1$^{S40A/T121A/S151A}$, Cdh1$^{S40A/T121A/S151A/S163A}$, Cdh1$^{T32A/S36A/S70A/S138A/S146A}$. All Cdh1 and its mutations were expressed in High 5 insect cells. To purify Cdh1, the cells were lysed in a buffer of 50 mM Tris.HCl (pH 7.3), 500 mM NaCl, 20 mM imidazole (Buffer A), with a protease inhibitor cocktail. After loading, the Ni-NTA column was washed with 10 column volumes of buffer A, followed by a gradient wash to 200 mM imidazole in buffer A and further washing with 10 column volumes of 200 mM imidazole in buffer A. The protein was eluted in buffer B of 300 mM imidazole (pH 7.3), 500 mM NaCl. Cdh1 was finally purified using S-200 size exclusion chromatography in 20 mM HEPES (pH 7.0), 200 mM NaCl, 1 mM DTT.

Human ubiquitin cDNA was cloned into a pET28 plasmid with an N-terminal His_6 tag and TEV cleavage site. Based on this plasmid, ubiquitin ^{I36A} and ubiquitin ^{I44A} mutants were prepared. Wild type and mutant ubiquitin were expressed in B834^{rare2} strain and purified by Ni-NTA and S75 size-exclusion chromatography (GE Healthcare).

APC/C Ubiquitination assays

Human APC/C and its different mutant derivatives, UBA1, UbcH10 and its mutants, Ube2S, ubiquitin and its mutants, and yeast Hsl1$^{667-872}$ were buffer exchanged into 20 mM HEPES (pH 8.0), 150 mM NaCl, 1 mM DTT. Human Cdh1 and its mutants were in 20 mM HEPES (pH 7.0), 200 mM NaCl, 1 mM DTT. Ubiquitination assays were performed as described [4]. For the UbcH10 competition assays, UbcH10 ^{C114K} and UbcH10 $^{C114K-LR}$ at the following concentrations (0.001, 0.01, 0.1, 1, 10 μM) were used to compete with UbcH10 (0.1 μM). Cdh1 was at 20 nM. To test the UbcH10-RING domain interface, the following UbcH10 and UbcH10^{LR} mutants were prepared and tested (Y91A and S123G). Single time point assays are at 10 mins.

Cdh1 Phosphorylation assays

CDK2-dependent phosphorylation of Cdh1 and its mutants was performed in buffer containing 50 mM HEPES (pH 8.0), 10 mM $MgCl_2$ 2mM ATP, 10 mM NaF, 10 mM glycerol phosphate, and 150 mM NaCl. The reactions were incubated at 23 °C for 30 min with 500 nM of Cdh1 and 50 nM of active phosphorylated CDK2-cyclin A3. The phosphorylation was terminated using the CDK1/2 inhibitor (Calbiochem). Non-CDK2 treated Cdh1 samples were set up in parallel with phosphorylating reactions by adding buffer instead of CDK2-cyclin A3. The activity assays were carried out as described for ubiquitination assays.

Peptide assays

Peptides for D box-lysine distance analysis were synthesized by Designer BioScience (Cambridge, UK). The peptides were modified by N-terminal biotinylation. Peptides used are Pep-1K: (EQRPRTALGDISNSKASGS), Pep-4K: (EQRPRTALGDISNSAGSKASGS), Pep-7K: (EQRPRTALGDISNSAGSAGSKASGS), Pep-10K (EQRPRTALGDISNSAGSAGSAGSKASGS), Pep-13K: (EQRPRTALGDISNSAGSAGSAGSAGSKASGS), Pep-18K: (EQRPRTALGDISNSAGSAGSAGSAGSAGSGSKASGS), GEM-K50: (EQRPRTALGDISNSASGSLVGRENELSAGLSKRRHR), and CycB-K64: (GLRPRTALGDIGNRVSEQLQARMPMRKEARPSATGS). The peptides were dissolved at a concentration of 6.25 mM in 100% DMSO. The ubiquitination assays were performed as described above except that 125 μM of peptide instead of Hsl1 was used as substrate. Previous work showed that at 100 μM D box-only peptides bind the D box receptor of APC/C^{Cdh1} (Refs [43,44]). The reactions were separated in 4-12% NuPAGE Bis-Tris gels (Life Technology) by 60 v for 2 h, followed by 150 v for 30 min for better resolution of peptides and ubiquitination products. After blotting, the membranes were blocked in 10% nonfat dry milk in PBS overnight at 4 °C. After washing the blot four times with PBS-2% Tween 20 buffer, ubiquitinated peptide products were visualized by Western blotting with PBS-buffered Streptavidin-HRP (Sigma) with 1% BSA.

Electron microscopy

Freshly purified recombinant human APC/C complexes (APC/$C^{Cdh1.Emi1}$, APC/$C^{Cdh1.Hsl1.UbcH10\text{-}Ub}$, and APC/$C^{Cdh1.Hsl1.Apc11\text{-}UbcH10}$) were first visualized by negative stain electron microscopy to check homogeneity. Complexes were then diluted to ~200 μg/ml and aliquots of 2 μl were applied to Quantifoil R2/2 grids coated with a second layer of home-made thin carbon film (estimated to be ~50 Å thick), treated with a 9:1 argon:oxygen plasma for 20 s before use. The grids were incubated for 30 s at 4 °C and 100% humidity and then blotted for 6 s and plunged into liquid ethane using an FEI Vitrobot III. The grids were loaded into an FEI Tecnai Polara electron microscope at an accelerating voltage of 300 kV. Images were taken manually using low-dose mode at a nominal magnification of × 78,000 (yielding a pixel size of 1.36 Å $pixel^{-1}$) for APC/$C^{Cdh1.Emi1}$ and APC/$C^{Cdh1.Hsl1.Apc11\text{-}UbcH10}$, and × 59,000 (yielding a pixel size of 1.77 Å $pixel^{-1}$) for APC/$C^{Cdh1.Hsl1.UbcH10\text{-}Ub}$. Images were recorded using a FEI Falcon II direct electron detector with a defocus range of ~2.5 to 4 μm. Each image was exposed for 2 s at dose rate of 27 $e^{-}/Å^2/s$ at a nominal magnification of × 78,000 and 16 $e^{-}/Å^2/s$ at a nominal magnification of × 59,000. 34 movie frames were recorded for each image as previously described [45].

To prepare a negative stain reconstruction of APC/$C^{Cdh1.Hsl1}$-UbcH10 (with excess wild type UbcH10), we incubated freshly purified APC/$C^{Cdh1.Hsl}$ (0.04 μM) with a 1500-fold excess of UbcH10 (60 μM, 200-fold in excess of K_d) for 1 h on ice. Images were collected on an FEI Spirit electron microscope at an accelerating voltage of 120 kV at −1.5 μm defocus. The map was reconstructed using RELION without CTF correction.

Image processing

All movie frames were first aligned by *motioncorr* program [46] before subsequent processing. Contrast transfer function parameters were calculated with CTFFING3 (Ref. [47]). Particles in 264×264 pixels (or 200×200 pixels for data collected at × 59,000 magnification) were initially selected automatically by *e2boxer.py* in EMAN2 (Ref. [48]) from a small portion of the same data set (typically ~300 micrographs). After 2D classification using RELION [49], 10 images in different views were selected from the 2D averages and used as reference for automatic particle picking for the whole data set by RELION 1.3 (Ref. [50]). The following procedures were performed in RELION to exclude bad particles from the final reconstruction. First, particles in each micrograph were displayed and manually screened to delete wrongly picked ice contamination. Secondly, extracted particles were sorted by similarity to reference images and particles with low Z scores were deleted (roughly ~10% particles were deleted in this step). Thirdly, 2D classification was performed and particles in bad classes (with poor structural features) were removed (roughly ~10-20% particles were deleted in this step). The resultant particles were then used for 3D classifications. Conformational heterogeneity and remaining bad particles were excluded from the final reconstruction in this step. A summary of particles used for final refinements is listed in Extended Data Table 1c.

Beam-induced particle motion was corrected using statistical movie processing in RELION as previous described [45]. For APC/C, a running average of 9 movie frames for frames within the first 32 e^{-} dose and a standard deviation of one pixel for the translational alignment were used. This step improved the resolution from 4.2 Å to 3.9 Å. Following this, *particle polishing* in RELION 1.3 were used to further improve the resolution [51]. This program fits all movie frames as linear tracks, considering movements of neighboring particles to improve signal for smaller particles. Furthermore, each frame is weighted by B-factor (estimated by each frame reconstruction) to treat radiation damage problem. Particle polishing was then used to improve the resolution from 3.9 Å to 3.6 Å. All resolution estimations were from gold-standard FSC calculations to avoid over-fitting and reported resolutions are based on the FSC = 0.143 criterion [52,53]. Final FSC curves were calculated using a soft spherical mask (with a 5-pixel fall-off) of the two independent reconstructions. To visualize high-resolution details, all density maps were corrected for modulation transfer function (MTF) of the detector and sharpened by applying negative B-factors, estimated using automated procedures [52].

Motion correction was performed after 3D classification for APC/$C^{Cdh1.Emi1}$ which showed ~ 60% ternary complex and ~ 40% apo state APC/C. For APC/$C^{Cdh1.Hsl1.UbcH10\text{-}Ub}$ and APC/$C^{Cdh1.Hsl1.Apc11\text{-}UbcH10}$, all particles were refined against one model and motion corrected as described above. The polished particles were used for 3D classification as shown in Extended Data Figure 6 and 7. The first cycle of classification was done by global search and sampling angular interval of 7.5° to sort out large conformational changes and cycle 2-4 were executed by local search within 15° and a smaller sampling angular interval of 3.7°. 3D classifications were run for 25 iterations with class number set at 10 and regularization parameter T set at 4.

Europe PMC Funders Author Manuscripts

To further improve the density map of flexible parts (RING domain and UbcH10) in the complexes, a soft mask was used for local alignment during refinement. A soft mask was generated according to combined coordinates of Apc1/Apc2/Apc4/Apc5/Apc11/UbcH10 (approximately half of the mass) and a restrained angular search of 3° was used. Local resolution was estimated using ResMap [54].

Model building of APC/C

Modelling of the structures of APC/C was performed in COOT [55]. Initially, available crystal structures and homology models as described in our previous work [4] were fitted into the cryo-EM map in Chimera. These structures include (1) crystal structures of human Apc10 (residues 2-162, PDB code: 1JHJ) [56], (2) N-terminal seven helices of Apc7 (residues 21-166, PDB code: 3FFL) [57], (3) *S. pombe* Cut9-Hcn26 complex (Apc6-Apc12 homologue, PDB code: 1XPI) [58], (4) N-terminal dimerization domains of *E. cuniculi* Cdc27 (Apc3 homologue, PDB code: 3KAE) [59] (5) *S. pombe* Cut23 (Apc8 homologue, PDB code: 3ZN3) [60], (6) Cdh1-D-KEN (PDB code: 4BH6) [39] (7) Apc5 TPR domain and C-terminal TPR helices of Apc3, Apc8 and Apc7 (model using the crystal structure of *S. pombe* Cut9 as template), (8) crystal structures of Apc4 and Apc5^{NTD} (residues 1-160) (unpublished data), (9) NMR structure of Emi1 ZBR domain [13] (PDB:2M6N) and Apc11 RING domain [26] (PDB code: 4R2Y). For Apc2-Apc11^{N}, the structure was modelled using a crystal structure of Cul1 (PDB code: 1U6G) [61] as a template. For Apc1 PC repeats, the structure was predicted with I-Tassar [62] using the PC domain structure of Rpn2 (PDB code: 4ADY) [63] as a reference. All fitted structures were rebuilt according to the cryo-EM map. The majority of Apc1, small subunits (Apc13, Apc15, Apc16), Ile-Arg (IR) C-terminal tails of Apc10 and Cdh1, N-terminal domain of Cdh1 (Cdh1^{NTD}) and some loops not seen in crystal structures and homology were built *ab initio*. Details given in Extended Data Table 2.

The model was refined by REFMAC v.5.8 (Ref. [64]). A REFMAC weight of 0.04 was defined by cross-validation using half reconstructions [65]. The resolution limit for refinement was set at 3.5 Å. All high-resolution crystal structures or NMR structures were used for secondary structure restraints. A summary of model refinement is listed in Extended Data Table 1a.

Rigid-body fitting was performed to UbcH10 by *'fit in map'* program in Chimera [66]. Crystal structure of Rnf4 - UbcH5a - ubiquitin heterotrimeric complex (PDB: 4AP4) [29] was used to model ubiquitin not seen directly from the reconstruction due to flexibility. A summary of model building is listed in Extended Data Table 2.

All regions of the APC/C EM density map were assigned to APC/C subunits. However, the intrinsically disordered regions of some APC/C subunits were not visible in the EM map (defined in Extended Data Table 2). Altogether, 78% APC/C residues were fitted to the EM map. Inter-subunit contact areas were calculated using CCP4 (Ref. [67]).

Map visualization

Figures and movie were generated using Pymol and Chimera [66].

Structural conservation was calculated using CONSURF [68] based on a multiple sequence alignment of *H. sapiens, M. musculus, X. laevis, C. elegans, D. melanogaster, A. thaliana, S. cerevisiae, S. pombe,* APC/C subunit sequences.

Protein similarity searches were performed using DALI [69], and protein alignment figures created using ALSCRIPT [70].

Extended Data

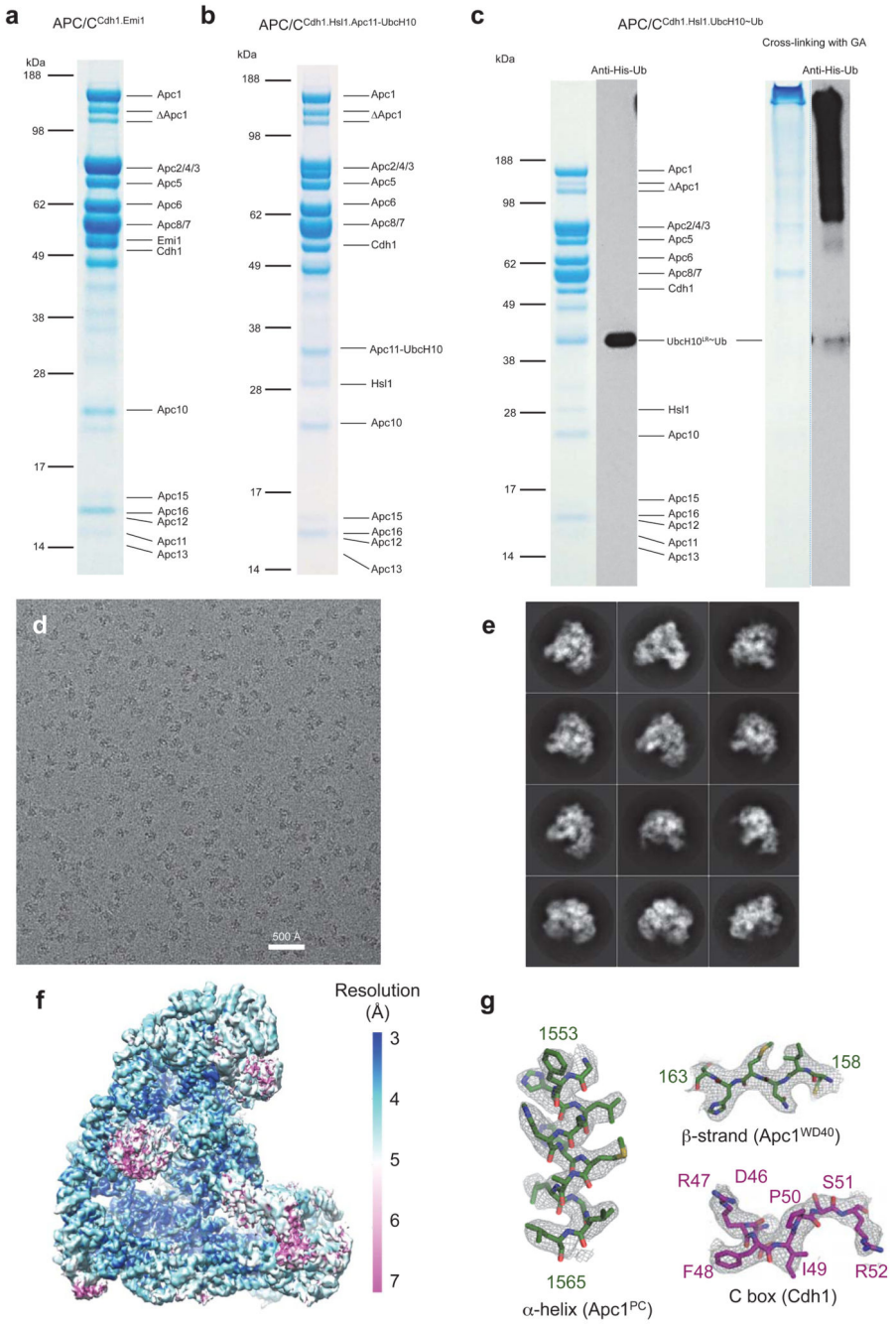

Europe PMC Funders Author Manuscripts

Europe PMC Funders Author Manuscripts

Extended Data Figure 1. Preparations and EM images of APC/C complexes

(a) Coomassie blue stained SDS gel of APC/$C^{Cdh1.Emi1}$. **(b)** Coomassie blue stained SDS gel of APC/$C^{Cdh1.Hsl1.Apc11\text{-}UbcH10}$. **(c)** Coomassie blue stained SDS gel and Western blot analysis (anti-His antibody - only ubiquitin in the complex contains His tag) of APC/$C^{Cdh1.Hsl1.UbcH10\text{-}Ub}$ without or with cross-linking by glutaraldehyde (GA). **(d)** A typical cryo-EM micrograph of APC/$C^{Cdh1.Emi1}$. Representative of 3328 micrographs. **(e)** Gallery of 2D averages of APC/$C^{Cdh1.Emi1}$ showing different views. Representative of 100 2D averages. (**f**) Local resolution map of APC/$C^{Cdh1.Emi1}$ showing resolution range. (**g**) Details of EM density for segments of α-helix and β-strand of Apc1 and the C box of Cdh1.

Europe PMC Funders Author Manuscripts

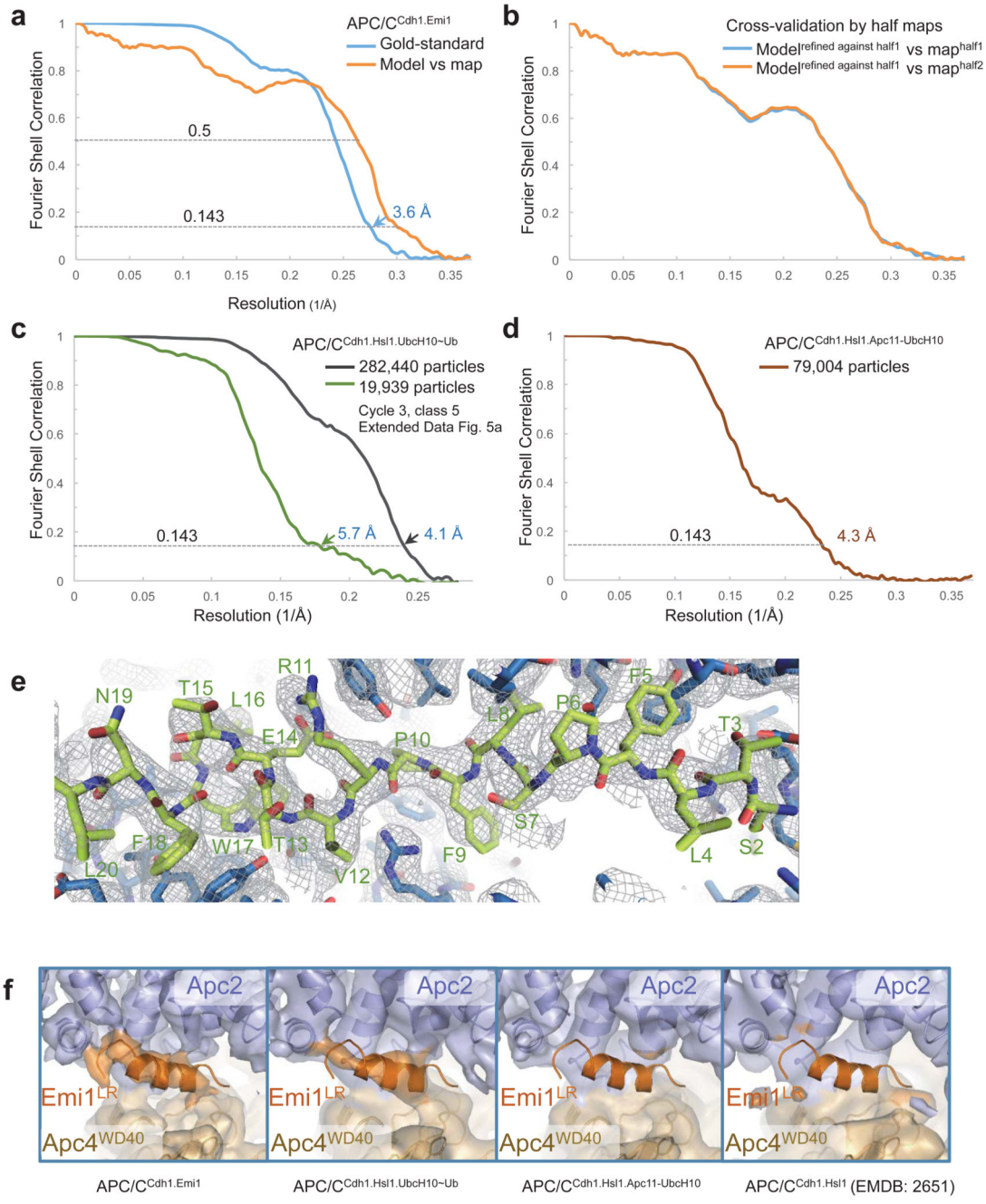

Extended Data Figure 2. Resolution estimation and example of *de novo* model building

(a) Gold standard Fourier Shell Correlation (FSC) curve and FSC curve between cryo-EM map and final atomic model of the APC/$C^{Cdh1.Emi1}$. **(b)** Cross-validation of model refinement by half maps. Shown are FSC curves between the atomic model and the half map (map^{half1}) it was refined against and FSC curve between the atomic model and the other half map (map^{half2}) that was not used during refinement. **(c)** Gold standard FSC curve of APC/$C^{Cdh1.Hsl1.UbcH10-Ub}$. **(d)** Gold standard FSC curves of human APC/$C^{Cdh1.Hsl1.Apc11-UbcH10}$. **(e)** *de novo* model building of Apc15 N-terminal loop. The surrounding Apc5 residues are

also shown. (**f**) EM density for the LR tail common to Emi1 and Ube2S is only observed in APC/C complexes with subunits incorporating the LR tail. (i) APC/C$^{Cdh1.Emi1}$. (ii) An APC/C complex with an LR tail-bearing subunit (UbcH10^{LR} of APC/C$^{Cdh1.Hsl1.UbcH10\text{-}Ub}$). (iii) No LR tail density in APC/C$^{Cdh1.Hsl1.Apc11\text{-}UbcH10}$ fusion and (iv) APC/C$^{Cdh1.Hsl1}$ (Ref. [4]).

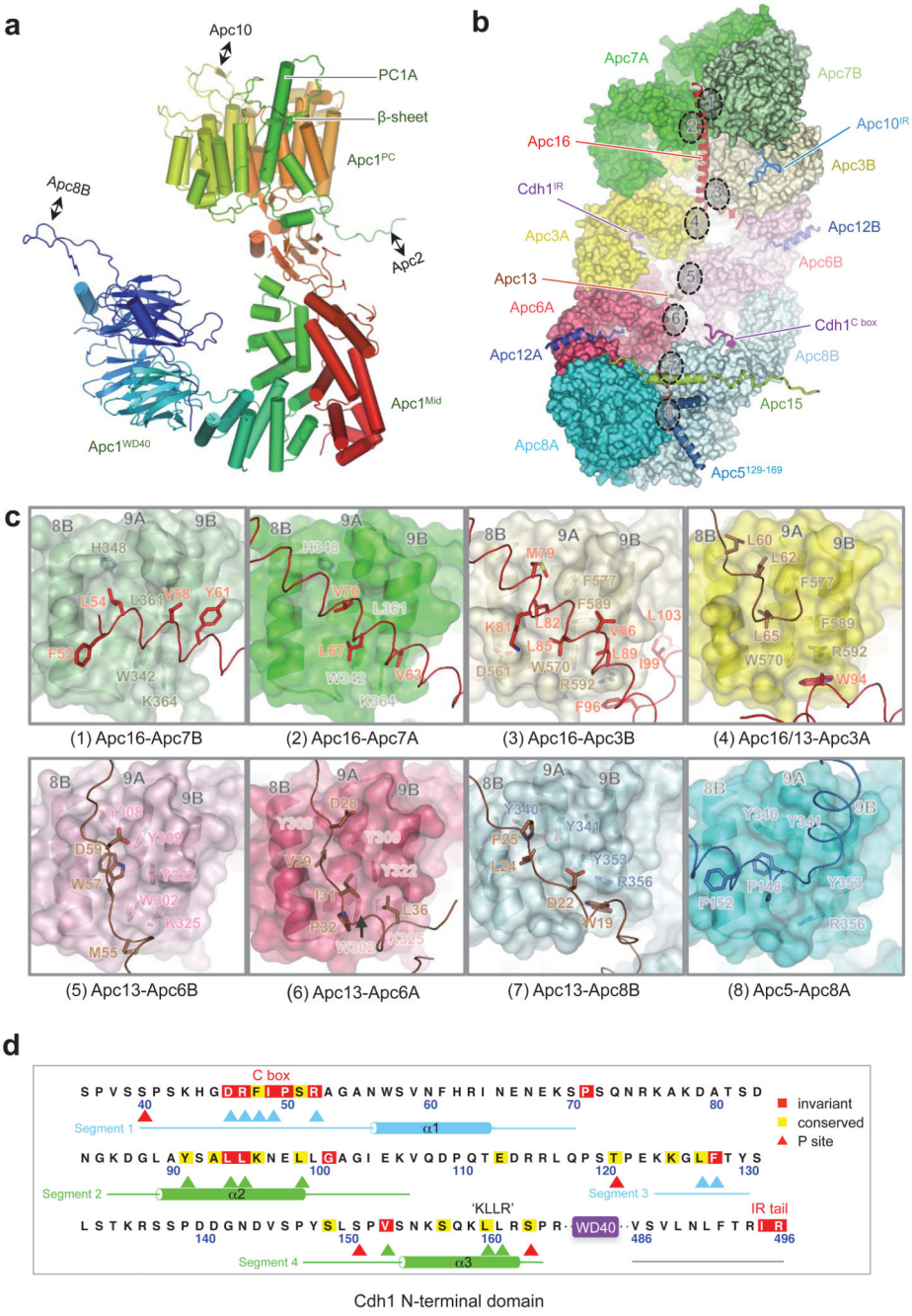

Extended Data Figure 3. Apc1 structure and the TPR lobe interacts with multiple subunits

(**a**) Cartoon of Apc1 colour-ramped from blue to red for N- to C-terminus. Insertions that interact with Apc2, Apc8 and Apc10 are labelled. Apc1^{Mid} adopts a novel architecture. (**b**) TPR lobe with TPR subunits shown as surface representations, with the small TPR-accessory subunits (Apc12, Apc13, Apc15 and Apc16), a segment of Apc5, an insert of Apc1, IR tails of Cdh1 and Apc10, and Cdh1 C box that interact with the TPR lobe are shown as cartoons. The N-termini of Apc12, Apc13 and Apc15 are buried. The eight structurally homologous and symmetry-equivalent sites on the TPR lobe that bind Apc13, Apc16 and Apc5 are indicated and shown in detail in (**c**). View is similar to Fig 1a. (**c**) The eight TPR subunits interact with Apc13, Apc16 and Apc5 mainly through contacts to four conserved aromatic residues present on most TPR subunits (Y308, Y309, W302, Y322 of Apc6 [panels 5 and 6]). (**d**) Sequence of the ordered region of Cdh1^{NTD} bound to Apc1 and Apc8 (ordered regions shown as lines and α-helices). Critical Apc1 and Apc8 contact residues are indicated with green and blue arrows. Phosphorylation sites indicated with red arrows.

Europe PMC Funders Author Manuscripts

Europe PMC Funders Author Manuscripts

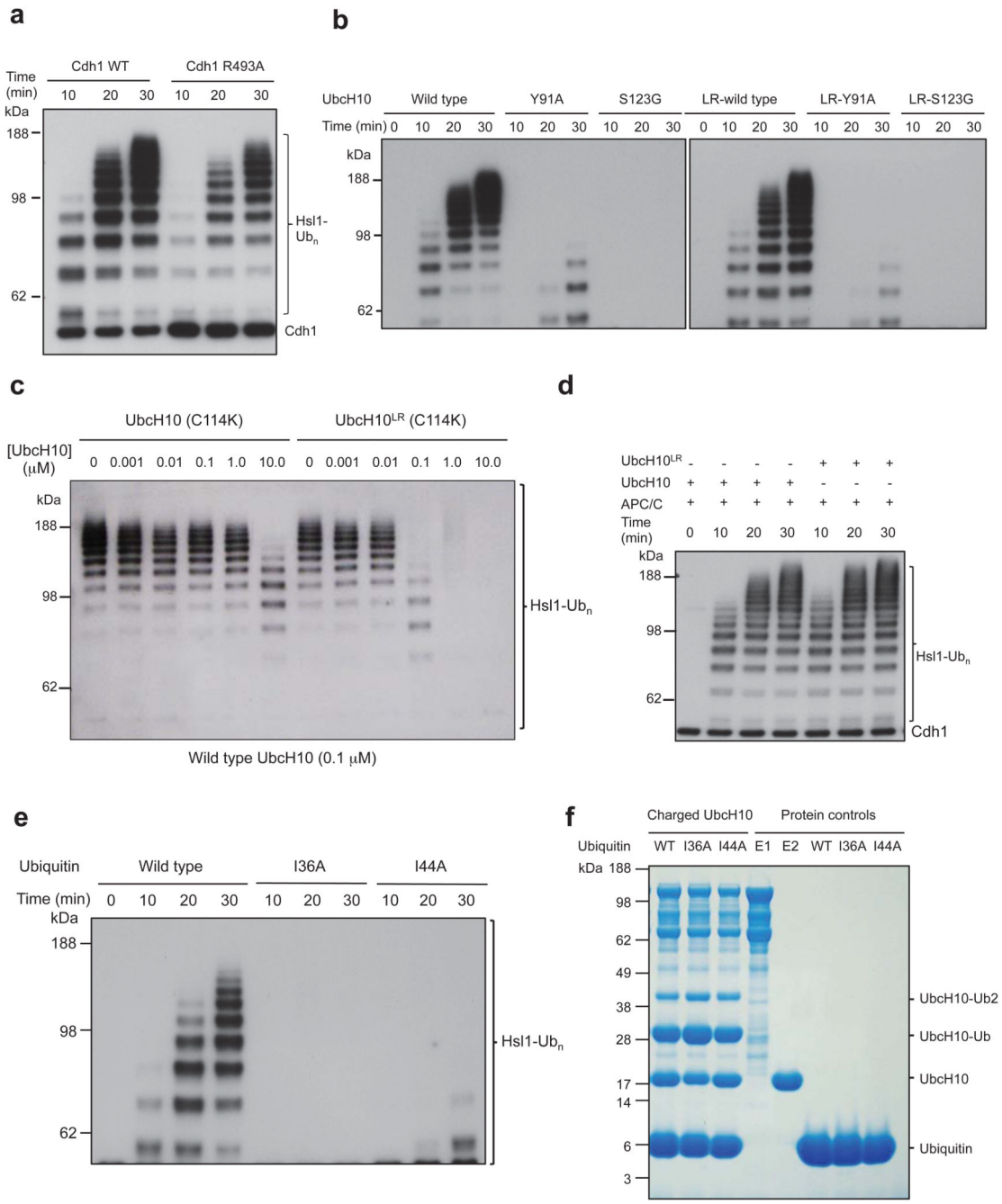

Extended Data Figure 4. APC/C ubiquitination assays

(**a**) Mutation of Arg493 of the IR tail reduces APC/C^{Cdh1} activity. (**b**) Mutations at the RING domain interface of UbcH10 and UbcH10^{LR} disrupt ubiquitination activity. (**c**) Ubiquitination assay shows that both UbcH10(C114K) and UbcH10^{LR}(C114K) compete with wild type UbcH10. UbcH10^{LR}(C114K) is a more potent inhibitor. **(d)** The APC/C-UbcH10-mediated substrate ubiquitination activities of UbcH10 and UbcH10^{LR} are indistinguishable. (**e**) The ubiquitin (I36A) and ubiquitin (I44A) mutants were defective for

APC/C-UbcH10-mediated substrate ubiquitination. (**f**) UbcH10 charging by the ubiquitin (I36A) and ubiquitin (I44A) mutants was unchanged relative to wild type ubiquitin.

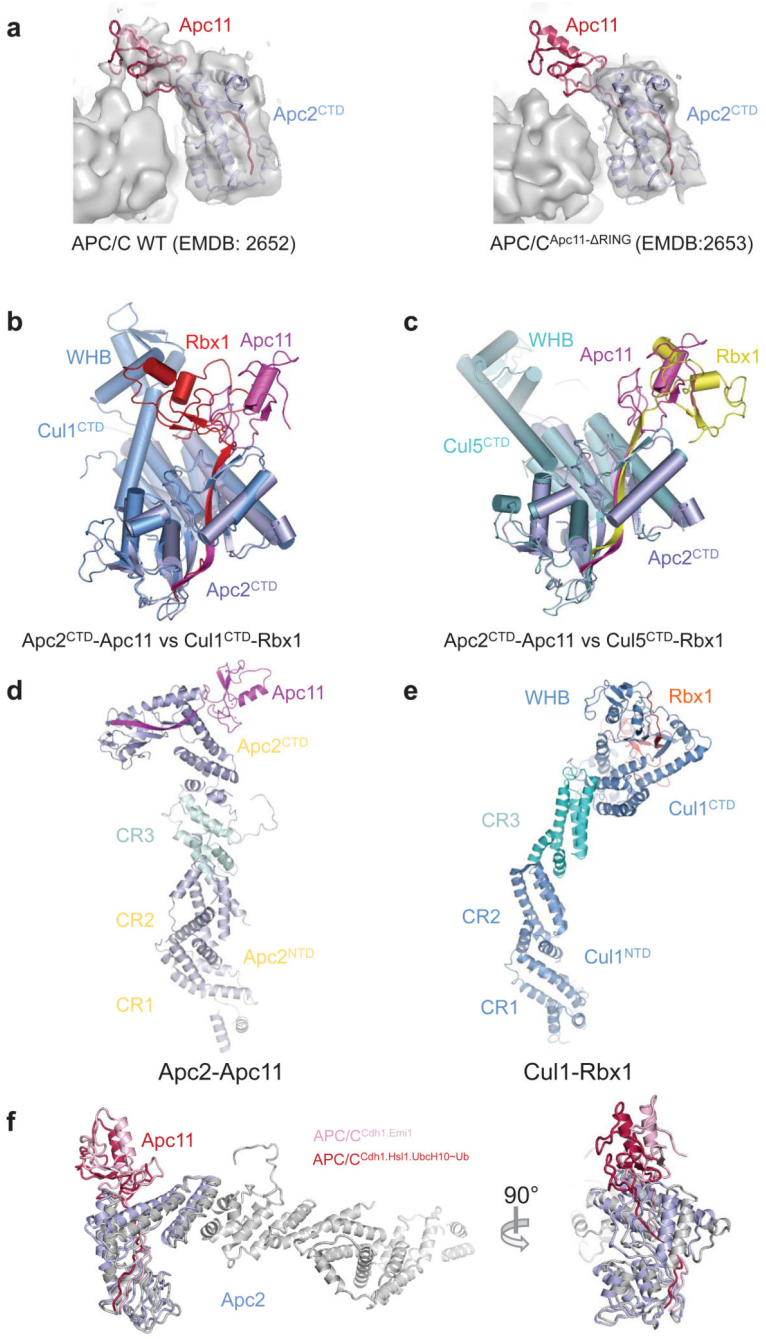

Extended Data Figure 5. The position of Apc11^{RING} in the APC/C is more similar to Rbx1^{RING} of activated cullin-Rbx1 structures

(**a**) Identification of Apc11 in apo APC/C. Left panel: EM density map for apo APC/C with the coordinates of Apc2^{CTD}-Apc11 fitted (from APC/C$^{Cdh1.Emi1}$ structure). Right panel. EM density for APC/C$^{Apc11-\Delta RING}$. The difference density corresponds to Apc11^{RING}. EM density maps from [4]. **(b)** Superimposed Apc2^{CTD} onto Cul1^{CTD} (PDB: 1LDK) [61]. **(c)**

Superimposed Apc2^{CTD} onto Cul5^{CTD} (PDB: 3DQV) [27]. In the inactive conformation of Cul1-Rbx1, Rbx1^{RING} packs against WHB. In APC/C$^{Cdh1.Emi1}$ the location of Apc11^{RING} remains in contact with Apc2^{CTD} but has rotated ~180° relative to inactive CRL structures being similar to the swung out conformation of Rbx1^{RING} of neddylated and activated Cul5-Rbx1 [27]. (**d and e**) The relative orientation of Apc2^{NTD} and Apc2^{CTD} is also dramatically different from Cul1 (Ref. [61]). This is due to a 70° rotation within cullin repeat 3 (between helices A-B and C-D-E), and a ~20° rotation around the 4HB - cullin repeat 3 interface. Similar less pronounced structural variations are observed within the CRL family. (**d**) Apc2-Apc11 (this study). (**e**) Cul1-Rbx1 (PDB: 1LDK) [61]. (**f**) The position of the Apc2^{CTD}-Apc11 module differs slightly about the Apc2^{NTD}-Apc2^{CTD} interface between APC/C$^{Cdh1.Emi1}$ and APC/C$^{Cdh1.Hsl1.UbcH10-Ub}$.

Europe PMC Funders Author Manuscripts

Europe PMC Funders Author Manuscripts

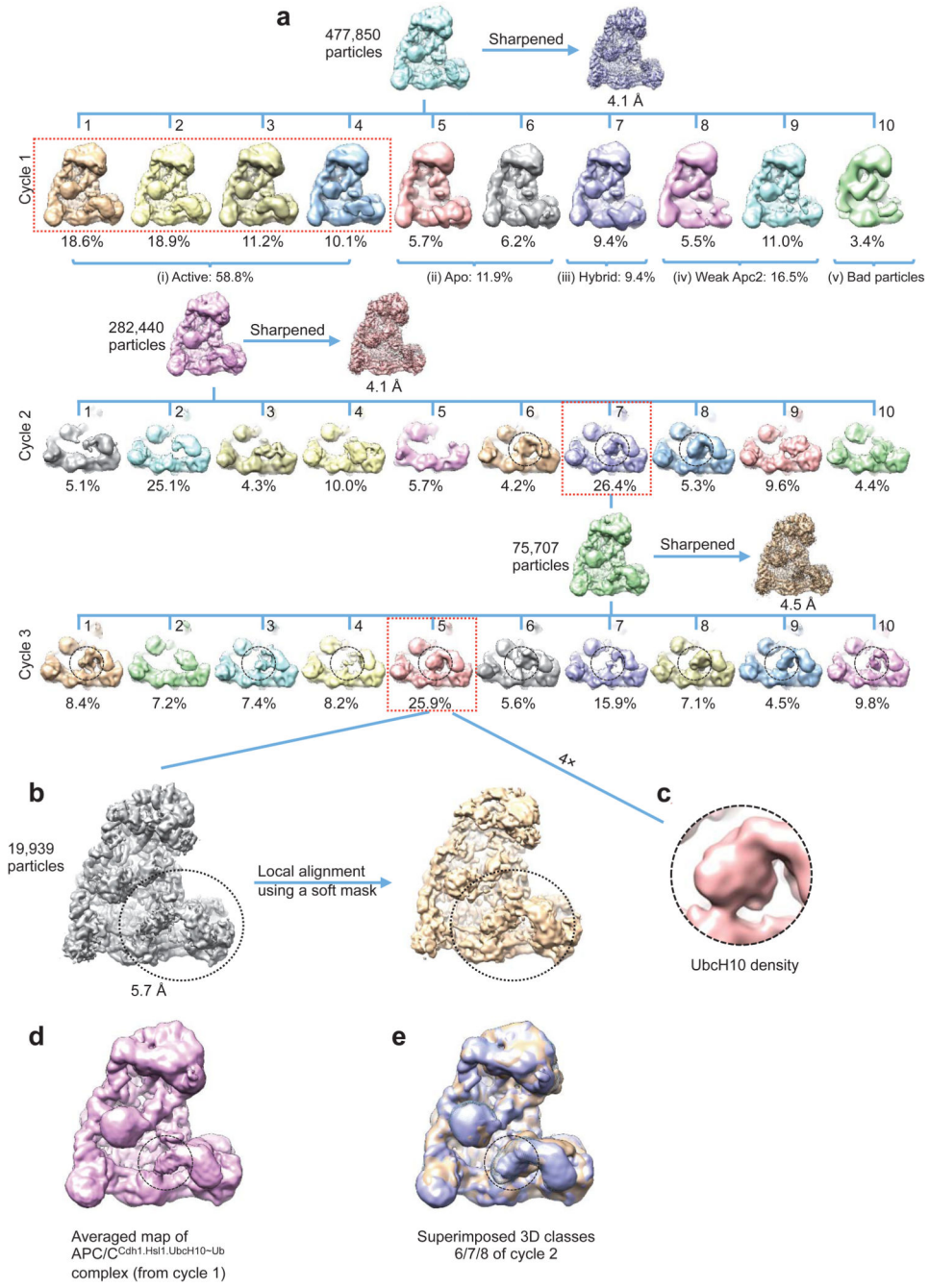

Extended Data Figure 6. Three dimensional classification of APC/C$^{Cdh1.Hsl1.UbcH10\text{-}Ub}$

(a) The 3D classification (Cycle 1) started with 477,850 motion corrected particles, which were divided into ten classes. The resultant classes were grouped into five categories: (i) 58.8% in the active ternary state with coactivator and substrate (Hsl1); (ii) 11.9% in the apo inactive state; (iii) 9.4% in a class with Cdh1 bound but with the catalytic module in the apo inactive conformation (hybrid state); (iv) 16.5% with weak Apc2 density and (v) 3.4% were a poor reconstruction due to bad particles. Examination of the hybrid state (iii) showed that density for Apc1^{WD40} was absent, explaining the lack of Cdh1-induced conformational

change of the catalytic module. Particles in the ternary state (reconstructed to an overall resolution of 4.1 Å) were subjected to further 3D classification (Cycle 2). A major class (class 7, 26.4% of particles) showed improved density for UbcH10 (circled) and Cycle 3 classification was performed on particles in this class. The major class of Cycle 3 (class 5, 25.9% particles) showed further improved UbcH10 density. Further 3D classification of this class did not improve the UbcH10 density. **(b)** Particles in the best class (Cycle 3, class 5, 19,939 particles) were refined in RELION and resulted in a map at 5.7 Å resolution (Extended Data Fig. 2c). The UbcH10 density was improved by local alignment using a soft mask (indicated by circles) as described in Methods. **(c)** Enlarged view of UbcH10 density. (**d**) Enlarged view of the averaged APC/$C^{Cdh1.Hsl1.UbcH10\text{-}Ub}$ reconstruction from cycle 1 of the 3D classification (59% of particles). UbcH10 density is circled. (**e**) Superimposition of classes 6, 7 and 8 of cycle 2 of the 3D classification (from (**a**)), showing the structural variability of the three 3D classes that indicate UbcH10 density. UbcH10 density is circled.

Europe PMC Funders Author Manuscripts

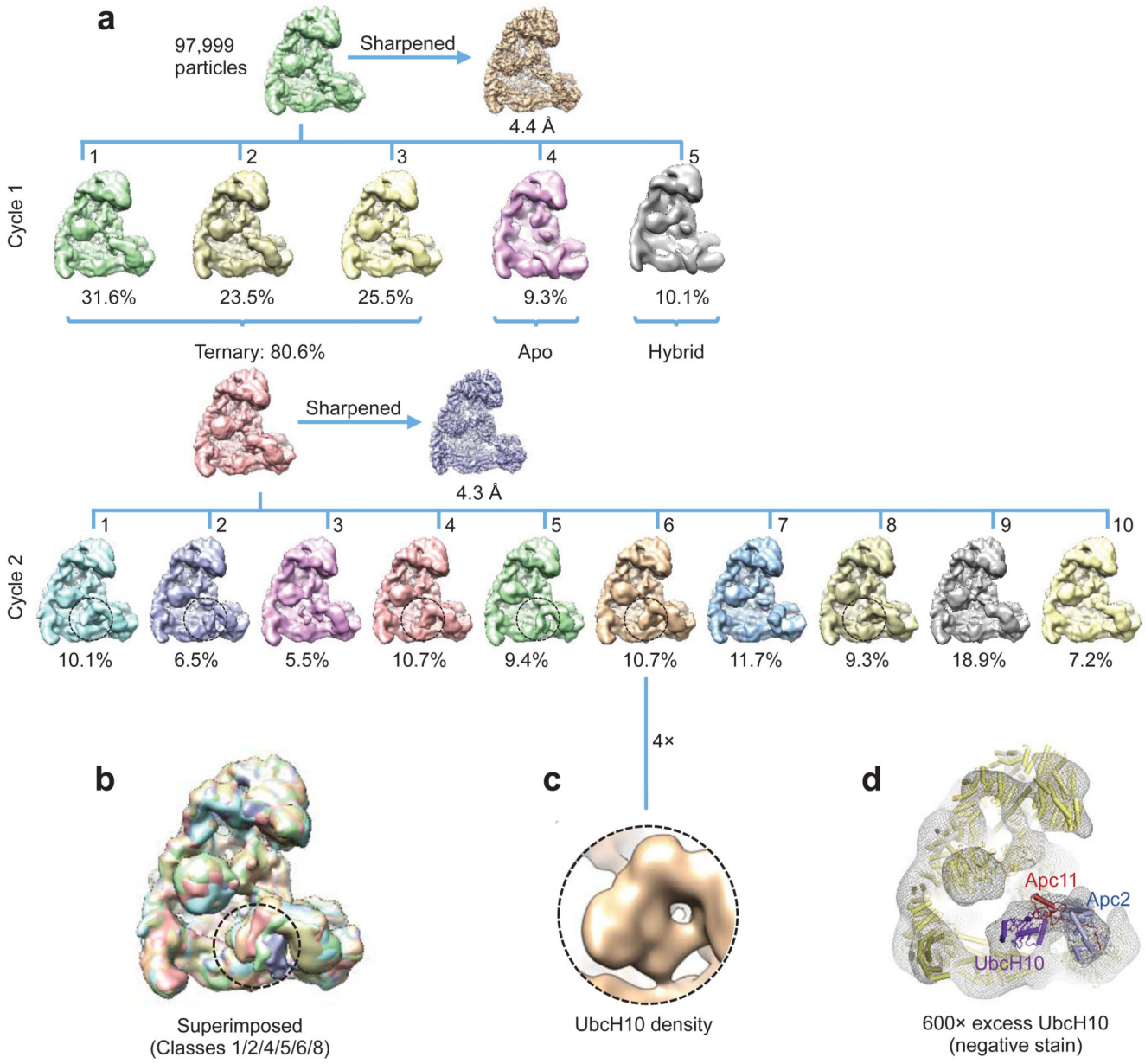

Extended Data Figure 7. Three dimensional classification of APC/C$^{Cdh1.Hsl1.Apc11-UbcH10}$

(a) The 3D classification started with 97,999 motion corrected particles, which were divided into five classes. The resultant classes were grouped into three categories: (i) 80.6% in the active ternary state with coactivator and substrate (Hsl1); (ii) 9.3% in the apo state and (iii) 10.1% in a hybrid state. Particles in the active ternary state (reconstructed to an overall resolution of 4.3 Å) were subjected to Cycle 2 classification with ten classes. UbcH10 density in the resultant classes is indicated with circles. **(b)** Classes with UbcH10 density in Cycle 2 classification are superimposed, showing variability of UbcH10. **(c)** Enlarged view of UbcH10 density. (**d**) A negative stain EM reconstruction of an APC/C$^{Cdh1.Hsl1}$ complex at ~25 Å resolution with a 1500-fold excess of UbcH10. The molecular surface is shown as

a mesh representation and the coordinates of the APC/C$^{Cdh1.Hsl1.UbcH10\text{-}Ub}$ were docked into the EM reconstruction. The UbcH10 coordinates fit new EM density proximal to Apc11.

Extended Data Table 1
Statistics of structure determination

a. Statistics of APC/C$^{Cdh1.Emi1}$ structure determination

Data collection	
EM:	FEI Polara, 300keV
Detector:	FEI Falcon II
Pixel size (Å):	1.36
Defocus range (μm):	1.5-4
Reconstruction	
Software:	RELION 1.3
Accuracy of rotations (degrees):	1.073
Accuracy of translations (pixels):	0.691
Final Resolution (Å):	3.6
Refinement	
Software:	RefMac 5.8
Refmac weight:	0.04
Resolution limits (Å):	3.5
Residue number	8408
Average Fourier shell correlation	0.8315
R factor:	0.222
Rms BondLength:	0.0135
Rms BondAngle:	1.8098
Validation	
Ramachandran plot:	
Preferred:	7669 (92.88%)
Allowed:	352 (4.26%)
Outliers:	236 (2.86%)

b. Statistics of all cryo-EM data

Samples	Micrographs	Particles (after movie correction)		Resolution (Å)
APC/C$^{Cdh1.Emi1}$	3328	In total:363,774		-
		Ternary	202,084 (55.6%)	3.6
		Apo	161,690 (44.4%)	4.3
		*Others (Hybrid, Weak Apc2 and Bad particles)	**52,178 particles deleted before movie correction*	-
APC/C$^{Cdh1.Hsl1}$-UbcH10^{RL}~Ub	4524	In total: 477,850		-
		Ternary	282,440 (59.1%)	4.1

Europe PMC Funders Author Manuscripts

Europe PMC Funders Author Manuscripts

b. Statistics of all cryo-EM data

Samples	Micrographs	Particles (after movie correction)		Resolution (Å)
		Apo	56,865 (11.9%)	-
		Others (Hybrid, Weak Apc2 and Bad particles)	138,545 (29.0%)	-
		In total: 97,999		-
		Ternary	79,004 (80.6%)	4.3
		Apo	9,114 (9.3%)	-
APC/C$^{Cdh1.Hsl1}$-UbcH10$^{Apc11-UbcH10}$	869	Others (Hybrid, Weak Apc2 and Bad particles)	9,801 (10.1%)	-

Europe PMC Funders Author Manuscripts

Extended Data Table 2

Summary of model building for APC/C subunits

Subunit	Length	Domain/Region 1	Domain/Region 2	Domain/Region 3	Disordered regions	Phosphorylation sites
Apc1	1,944	WD40 domain (1-612) De novo	Mid-N (613-986) Mid-C (1617-1944) De novo	PC domain (1013-1616) Homology. PDB: 4ADY Inserts: De novo	1-10,59-70,135-145,193-205,227-235,296-401,415-423,514-581,671-756,815-838,883-923,987-1012,1334-1346,1438-1451,1712-1726,1930-1944	202,286,291,341,343,355, 362,364,373,377,537,571,681, 688
Apc2	822	NTD (1-432) Homology. PDB: 1LDK	CTD(433-822) Homology. PDB: 1LDK	-	1-14, 30-52,66-69,103-106, 192-195, 221-231,305-319,444-450,459-475 731-822 (WHB)	218,314,532,534
Apc3	824	TPR dimer interface TPR motifs 1-7 (1-535) Homology. PDB: 3KAE	TPR superhelix TPR motifs 8-14 (536-824) Homology. PDB: 2XPI	-	171-450,767-824 (A) 171-450,782-824 (B)	205,209,220,244,264,291, 302,304,313,334,336,364, 366,369,383,384,386,426, 430,435,438,446,447
Apc4	808	WD40 domain/4HB X ray: unpublished Inserts: De novo	-	-	429-438,458-469,758-808	469,777
Apc5	755	NTD (1-169) X ray: unpublished	TPR superhelix TPR motifs 1-13 (206-755) Homology. PDB: 2XPI Inserts: De novo	-	1-26,170-205	15,232,195
Apc6	620	TPR dimer interface TPR motifs 1-7 (1-261) Homology. PDB: 2XPI	TPR superhelix TPR motifs 8-14 (262-620) Homology. PDB: 3HYM	-	96-126,528-620 (A) 96-123,534-620 (B)	112,490,559,560,580,581, 585,586,599
Apc7	599	TPR dimer interface TPR motifs 1-3 (21-166) X ray. PDB: 3FFL	TPR dimer interface TPR motifs 4-7 (167-359) Homology. PDB: 2XPI	TPR superhelix TPR motifs 8-14 (360-599) Homology. PDB: 2XPI	1-35,111-131,553-599 (A) 1-35,111-131,541-599 (B)	51,57,64,119,120,125
Apc8	597	TPR dimer interface TPR motifs 1-7 (1-287) Homology. PDB: 3ZN3	TPR superhelix TPR motifs 8-14 (288-597) Homology. PDB: 2XPI	-	1-25,501-508,558-597 (A) 1-25,501-508,558-597 (B)	267,556,576,578,582,590
Apc10	185	Doc homology (2-162) X-ray. PDB: 1JHJ	IR tail (163-185) De novo	-	-	-
Apc11	84	β-strand (1-18) Homology. PDB: 1LDK	RING domain (21-84) X-ray. PDB: 4R2Y	-	-	-
Apc12	85	N-term (1-25) X-ray. PDB: 3HYM	-	-	26-85	-
Apc13	74	De novo	-	-	40,47,68-79	
Apc15	121	De novo	-	-	57-121	-
Apc16	110	De novo	-	-	1-51	

Europe PMC Funders Author Manuscripts

Subunit	Length	Domain/Region 1	Domain/Region 2	Domain/Region 3	Disordered regions	Phosphorylation sites
Cdh1	496	NTD (1-163) De novo	WD40 domain (169-470) Homology: 4BHY	IR tail (483-496) De novo	1-41,68-87,109-124,133-145,164-168,471-482	-
Emi1	447	D box (319-335) X ray/De novo	ZBR (356-372) NMR. PDB: 2M6N	Linker (356-372), De novo LR tail (431-447), De novo	1-318,336-355,373-430	-
UbcH10	179	UBC domain (30-179) X-ray. PDB: 1I7K	-	-	1-29	-
Ubiquitin	76	X-ray. PDB: 4ADY	-	-	-	-

Phosphorylation site data from 71-73.

Europe PMC Funders Author Manuscripts

Extended Data Table 3

a. Inter-subunit contact surface area Å².

Subunit	Apc1	Apc2	Apc3	Apc4	Apc5	Apc6	Apc7	Apc8	Apc10	Apc11	Apc12	Apc13	Apc15	Apc16	Cdh1	Emi1
Apc1	-															
Apc2	2520	-														
Apc3	360	0	5746													
Apc4	0	714	0	-												
Apc5	8744	0	0	6226	-											
Apc6	1056	0	4590	0	0	5244										
Apc7	0	0	5354	0	0	0	5026									
Apc8	4290	0	0	0	3722	3772	0	4558								
Apc10	2616	0	2510	0	0	0	0	0	-							
Apc11	0	3402	0	0	0	0	0	0	0	-						
$Apc11^{RING}$	0	666	0	0	0	0	0	0	0	0						
Apc12	246	0	0	0	0	5970	0	0	0	0	-					
Apc13	0	0	836	0	0	2068	0	3240	0	0	0	-				
Apc15	0	0	0	224	3446	340	0	1082	0	0	0	0	-			
Apc16	40	0	2514	0	0	222	1502	0	0	0	0	0	0	-		
Cdh1	1960	0	1906	0	0	712	0	3022	0	0	0	0	0	0	-	
$Cdh1^{NTD}$	1960	0	0	0	0	500	0	3022	0	0	0	0	0	0	0	0
$Cdh1^{WD40}$	0	0	82	0	0	212	0	0	0	0	0	0	0	0	0	0
Cdh1IR	0	0	1824	0	0	0	0	0	0	0	0	0	0	0	0	0
Emi1	732	762	0	0	0	0	0	0	704	1300	0	0	0	0	754	-
Total	24524	8064	25722	7164	34010	24686	11882	26708	5830	4702	6216	6144	5092	4278	8354	4252

b. DALI Results

Subunit/domain	Protein match	RCSB PDB	Z	RMSD Å	Aligned N	Res N	ID %	Subunit/domain	Protein match	RCSB PDB	Z	RMSD Å	Aligned N	Res N	ID %
$Apc1^{WD40}$	*Sc* Cdh1	4BH6-E	15.9	4.0	259	303	8	Apc6	*Sp* Apc6	2XPI-D	36.9	2.2	481	520	37
$Apc1^{PC}$	*Sc* Rpn2	4ADY-B	27.8	3.2	406	802	15	Apc7	*Sp* Apc6	2XPI-D	24.9	7.8	464	518	15
$Apc2^{NTD}$	*Hs* Cul3	4HXI-B	13.8	7.4	301	346	7	Apc8	*Sp* Apc6	2XPI-D	25.5	7.2	443	518	19

Europe PMC Funders Author Manuscripts

b. DALI Results

Subunit/domain	Protein match	RCSB PDB	Z	RMSD Å	Aligned N	Res N	ID %	Subunit/domain	Protein match	RCSB PDB	Z	RMSD Å	Aligned N	Res N	ID %
Apc2^{CTD}	*Hs* Cullin1	4F52-A	23.5	2.2	237	258	18	Apc3A	Apc3B	-		1.6	482	497	100
Apc5^{TPR}	*Sp* Apc6	2XPI-A						Apc6A	Apc6B	-		4.0	486	503	100
Apc3	*Sp* Apc6	2XPI-A	29.6	4.9	456	518	19	Apc7A	Apc7B	-		2.6	483	483	100
								Apc8A	Apc8B	-		3.7	389	490	100

c. Surface Plasma Resonance Data

Ligand	Analyte	k_{off} (s^{-1})	k_{on} (M^{-1} s^{-1})	K^{eq}_d (nM)	K^{kin}_d (nM)	Reference
UbcH10	Ternary	0.42 ± 0.02	1.78 ± 0.2 × 10^6	215	236 ± 29	4
UbcH10^{LR}	Ternary (fast)	4.0 ± 0.2 × 10^{-2}	1.70 ± 0.1 × 10^6	31	24 ± 2	This study
	(slow)	4.6 ± 0.2 × 10^{-3}	1.70 ± 0.1 × 10^5		23 ± 5	

K^{kin}_d is the ratio of the observed microscopic rate constants.

Calculated using CCP4. **(b) Pair-wise structural comparison (DALI) of APC/C subunits. (c) Surface Plasma Resonance data.** Table comparing APC/$^{CCdh1.Hsl1}$ (ternary APC/C), dissociation constants for UbcH10 (Ref. 4), and UbcH10^{LR} (this work). K^{eq}_d: Equilibrium dissociation constant; K^{kin}_d: kinetic dissociation constant = k_{off}/k_{on}. Standard errors of the fit are listed.

Supplementary Material

Refer to Web version on PubMed Central for supplementary material.

Acknowledgments

This work was funded by a Cancer Research UK grant to DB. We thank W.J. Chazin and members of the Barford group for helpful discussions, and X. Bai and S. Scheres for their help with RELION; C. Savva and S. Chen for EM facilities; P. Emsley for help with COOT; G. Murshudov for help with REFMAC; G. McMullan for his assistance in movie data capture; J. Grimmett and T. Darling for computing and A. Boland for advice with COOT and PyMol.

References

1. Meyer HJ, Rape M. Processive ubiquitin chain formation by the anaphase-promoting complex. Seminars in cell & developmental biology. 2011; 22:544–550. [PubMed: 21477659]
2. Pines J. Cubism and the cell cycle: the many faces of the APC/C. Nat Rev Mol Cell Biol. 2011; 12:427–438. [PubMed: 21633387]
3. Primorac I, Musacchio A. Panta rhei: the APC/C at steady state. The Journal of cell biology. 2013; 201:177–189. [PubMed: 23589490]
4. Chang L, Zhang Z, Yang J, McLaughlin SH, Barford D. Molecular architecture and mechanism of the anaphase-promoting complex. Nature. 2014; 513:388–393. [PubMed: 25043029]
5. Kimata Y, Baxter JE, Fry AM, Yamano H. A role for the Fizzy/Cdc20 family of proteins in activation of the APC/C distinct from substrate recruitment. Molecular cell. 2008; 32:576–583. [PubMed: 19026787]
6. Van Voorhis VA, Morgan DO. Activation of the APC/C ubiquitin ligase by enhanced E2 efficiency. Current biology: CB. 2014; 24:1556–1562. [PubMed: 24930963]
7. Kelly A, Wickliffe KE, Song L, Fedrigo I, Rape M. Ubiquitin chain elongation requires e3-dependent tracking of the emerging conjugate. Molecular cell. 2014; 56:232–245. [PubMed: 25306918]
8. Kramer ER, Scheuringer N, Podtelejnikov AV, Mann M, Peters JM. Mitotic regulation of the APC activator proteins CDC20 and CDH1. Molecular biology of the cell. 2000; 11:1555–1569. [PubMed: 10793135]
9. Rudner AD, Murray AW. Phosphorylation by Cdc28 activates the Cdc20-dependent activity of the anaphase-promoting complex. The Journal of cell biology. 2000; 149:1377–1390. [PubMed: 10871279]
10. Jaspersen SL, Charles JF, Morgan DO. Inhibitory phosphorylation of the APC regulator Hct1 is controlled by the kinase Cdc28 and the phosphatase Cdc14. Current biology: CB. 1999; 9:227–236. [PubMed: 10074450]
11. Zachariae W, Schwab M, Nasmyth K, Seufert W. Control of cyclin ubiquitination by CDK-regulated binding of Hct1 to the anaphase promoting complex. Science. 1998; 282:1721–1724. [PubMed: 9831566]
12. Reimann JD, et al. Emi1 is a mitotic regulator that interacts with Cdc20 and inhibits the anaphase promoting complex. Cell. 2001; 105:645–655. [PubMed: 11389834]
13. Frye JJ, et al. Electron microscopy structure of human APC/C(CDH1)-EMI1 reveals multimodal mechanism of E3 ligase shutdown. Nature structural & molecular biology. 2013; 20:827–835.
14. Wang W, Kirschner MW. Emi1 preferentially inhibits ubiquitin chain elongation by the anaphase-promoting complex. Nature cell biology. 2013; 15:797–806. [PubMed: 23708001]
15. Wickliffe KE, Lorenz S, Wemmer DE, Kuriyan J, Rape M. The mechanism of linkage-specific ubiquitin chain elongation by a single-subunit e2. Cell. 2011; 144:769–781. [PubMed: 21376237]
16. Williamson A, et al. Identification of a physiological E2 module for the human anaphase-promoting complex. Proceedings of the National Academy of Sciences of the United States of America. 2009; 106:18213–18218. [PubMed: 19822757]

17. Wu T, et al. UBE2S drives elongation of K11-linked ubiquitin chains by the anaphase-promoting complex. Proceedings of the National Academy of Sciences of the United States of America. 2010; 107:1355–1360. [PubMed: 20080579]
18. Sironi L, et al. Crystal structure of the tetrameric Mad1-Mad2 core complex: implications of a 'safety belt' binding mechanism for the spindle checkpoint. The EMBO journal. 2002; 21:2496–2506. [PubMed: 12006501]
19. Izawa D, Pines J. Mad2 and the APC/C compete for the same site on Cdc20 to ensure proper chromosome segregation. The Journal of cell biology. 2012; 199:27–37. [PubMed: 23007648]
20. Thornton BR, et al. An architectural map of the anaphase-promoting complex. Genes & development. 2006; 20:449–460. [PubMed: 16481473]
21. Matyskiela ME, Morgan DO. Analysis of activator-binding sites on the APC/C supports a cooperative substrate-binding mechanism. Molecular cell. 2009; 34:68–80. [PubMed: 19362536]
22. Izawa D, Pines J. How APC/C-Cdc20 changes its substrate specificity in mitosis. Nature cell biology. 2011; 13:223–233. [PubMed: 21336306]
23. Sikorski RS, Michaud WA, Hieter P. p62cdc23 of Saccharomyces cerevisiae: a nuclear tetratricopeptide repeat protein with two mutable domains. Mol Cell Biol. 1993; 13:1212–1221. [PubMed: 8423787]
24. Lukas C, et al. Accumulation of cyclin B1 requires E2F and cyclin-A-dependent rearrangement of the anaphase-promoting complex. Nature. 1999; 401:815–818. [PubMed: 10548110]
25. Miller JJ, et al. Emi1 stably binds and inhibits the anaphase-promoting complex/cyclosome as a pseudosubstrate inhibitor. Genes & development. 2006; 20:2410–2420. [PubMed: 16921029]
26. Brown NG, et al. Mechanism of Polyubiquitination by Human Anaphase-Promoting Complex: RING Repurposing for Ubiquitin Chain Assembly. Molecular cell. 2014
27. Duda DM, et al. Structural insights into NEDD8 activation of cullin-RING ligases: conformational control of conjugation. Cell. 2008; 134:995–1006. [PubMed: 18805092]
28. Meyer HJ, Rape M. Enhanced protein degradation by branched ubiquitin chains. Cell. 2014; 157:910–921. [PubMed: 24813613]
29. Plechanovova A, Jaffray EG, Tatham MH, Naismith JH, Hay RT. Structure of a RING E3 ligase and ubiquitin-loaded E2 primed for catalysis. Nature. 2012; 489:115–120. [PubMed: 22842904]
30. Dou H, Buetow L, Sibbet GJ, Cameron K, Huang DT. BIRC7-E2 ubiquitin conjugate structure reveals the mechanism of ubiquitin transfer by a RING dimer. Nature structural & molecular biology. 2012; 19:876–883.
31. Ozkan E, Yu H, Deisenhofer J. Mechanistic insight into the allosteric activation of a ubiquitin-conjugating enzyme by RING-type ubiquitin ligases. Proceedings of the National Academy of Sciences of the United States of America. 2005; 102:18890–18895. [PubMed: 16365295]
32. Saha A, Lewis S, Kleiger G, Kuhlman B, Deshaies RJ. Essential role for ubiquitin-ubiquitin-conjugating enzyme interaction in ubiquitin discharge from Cdc34 to substrate. Molecular cell. 2011; 42:75–83. [PubMed: 21474069]
33. Pruneda JN, et al. Structure of an E3:E2~Ub complex reveals an allosteric mechanism shared among RING/U-box ligases. Molecular cell. 2012; 47:933–942. [PubMed: 22885007]
34. Dou H, Buetow L, Sibbet GJ, Cameron K, Huang DT. Essentiality of a non-RING element in priming donor ubiquitin for catalysis by a monomeric E3. Nature structural & molecular biology. 2013; 20:982–986.
35. Scott DC, et al. Structure of a RING E3 trapped in action reveals ligation mechanism for the ubiquitin-like protein NEDD8. Cell. 2014; 157:1671–1684. [PubMed: 24949976]
36. Reverter D, Lima CD. Insights into E3 ligase activity revealed by a SUMO-RanGAP1-Ubc9-Nup358 complex. Nature. 2005; 435:687–692. [PubMed: 15931224]
37. Soss SE, Klevit RE, Chazin WJ. Activation of UbcH5c~Ub is the result of a shift in interdomain motions of the conjugate bound to U-box E3 ligase E4B. Biochemistry. 2013; 52:2991–2999. [PubMed: 23550736]
38. Williamson A, et al. Regulation of ubiquitin chain initiation to control the timing of substrate degradation. Molecular cell. 2011; 42:744–757. [PubMed: 21700221]

39. He J, et al. Insights into Degron Recognition by APC/C Coactivators from the Structure of an Acm1-Cdh1 Complex. Molecular cell. 2013; 50:649–660. [PubMed: 23707760]
40. Izawa D, Pines J. The mitotic checkpoint complex binds a second CDC20 to inhibit active APC/C. Nature. 2014
41. Zeng X, et al. Pharmacologic inhibition of the anaphase-promoting complex induces a spindle checkpoint-dependent mitotic arrest in the absence of spindle damage. Cancer cell. 2010; 18:382–395. [PubMed: 20951947]
42. Zhang Z, et al. Recombinant expression, reconstitution and structure of human anaphase-promoting complex (APC/C). The Biochemical journal. 2013; 449:365–371. [PubMed: 23078409]
43. Kraft C, Vodermaier HC, Maurer-Stroh S, Eisenhaber F, Peters JM. The WD40 propeller domain of Cdh1 functions as a destruction box receptor for APC/C substrates. Molecular cell. 2005; 18:543–553. [PubMed: 15916961]
44. da Fonseca PC, et al. Structures of APC/C(Cdh1) with substrates identify Cdh1 and Apc10 as the D-box co-receptor. Nature. 2011; 470:274–278. [PubMed: 21107322]
45. Bai XC, Fernandez IS, McMullan G, Scheres SH. Ribosome structures to near-atomic resolution from thirty thousand cryo-EM particles. eLife. 2013; 2:e00461. [PubMed: 23427024]
46. Li X, et al. Electron counting and beam-induced motion correction enable near-atomic-resolution single-particle cryo-EM. Nature methods. 2013; 10:584–590. [PubMed: 23644547]
47. Mindell JA, Grigorieff N. Accurate determination of local defocus and specimen tilt in electron microscopy. Journal of structural biology. 2003; 142:334–347. [PubMed: 12781660]
48. Tang G, et al. EMAN2: an extensible image processing suite for electron microscopy. Journal of structural biology. 2007; 157:38–46. [PubMed: 16859925]
49. Scheres SH. RELION: implementation of a Bayesian approach to cryo-EM structure determination. Journal of structural biology. 2012; 180:519–530. [PubMed: 23000701]
50. Scheres SH. Semi-automated selection of cryo-EM particles in RELION-1.3. Journal of structural biology. 2014
51. Scheres SH. Beam-induced motion correction for sub-megadalton cryo-EM particles. eLife. 2014; 3:e03665. doi:10.7554/eLife.03665. [PubMed: 25122622]
52. Rosenthal PB, Henderson R. Optimal determination of particle orientation, absolute hand, and contrast loss in single-particle electron cryomicroscopy. Journal of molecular biology. 2003; 333:721–745. [PubMed: 14568533]
53. Scheres SH, Chen S. Prevention of overfitting in cryo-EM structure determination. Nature methods. 2012; 9:853–854. [PubMed: 22842542]
54. Kucukelbir A, Sigworth FJ, Tagare HD. Quantifying the local resolution of cryo-EM density maps. Nature methods. 2014; 11:63–65. [PubMed: 24213166]
55. Emsley P, Cowtan K. Coot: model-building tools for molecular graphics. Acta Crystallogr D Biol Crystallogr. 2004; 60:2126–2132. [PubMed: 15572765]
56. Wendt KS, et al. Crystal structure of the APC10/DOC1 subunit of the human anaphase-promoting complex. Nat Struct Biol. 2001; 8:784–788. [PubMed: 11524682]
57. Han D, et al. Crystal structure of the N-terminal domain of anaphase-promoting complex subunit 7. The Journal of biological chemistry. 2009; 284:15137–15146. [PubMed: 19091741]
58. Zhang Z, Kulkarni K, Hanrahan SJ, Thompson AJ, Barford D. The APC/C subunit Cdc16/Cut9 is a contiguous tetratricopeptide repeat superhelix with a homo-dimer interface similar to Cdc27. The EMBO journal. 2010; 29:3733–3744. [PubMed: 20924356]
59. Zhang Z, et al. Molecular structure of the N-terminal domain of the APC/C subunit Cdc27 reveals a homo-dimeric tetratricopeptide repeat architecture. Journal of molecular biology. 2010; 397:1316–1328. [PubMed: 20206185]
60. Zhang Z, et al. The four canonical tpr subunits of human APC/C form related homo-dimeric structures and stack in parallel to form a TPR suprahelix. Journal of molecular biology. 2013; 425:4236–4248. doi:10.1016/j.jmb.2013.04.004. [PubMed: 23583778]
61. Zheng N, et al. Structure of the Cul1-Rbx1-Skp1-F boxSkp2 SCF ubiquitin ligase complex. Nature. 2002; 416:703–709. [PubMed: 11961546]

62. Roy A, Kucukural A, Zhang Y. I-TASSER: a unified platform for automated protein structure and function prediction. Nature protocols. 2010; 5:725–738. [PubMed: 20360767]
63. He J, et al. The structure of the 26S proteasome subunit Rpn2 reveals its PC repeat domain as a closed toroid of two concentric alpha-helical rings. Structure. 2012; 20:513–521. [PubMed: 22405010]
64. Murshudov GN, et al. REFMAC5 for the refinement of macromolecular crystal structures. Acta Crystallogr D Biol Crystallogr. 2011; 67:355–367. [PubMed: 21460454]
65. Fernandez IS, Bai XC, Murshudov G, Scheres SH, Ramakrishnan V. Initiation of translation by cricket paralysis virus IRES requires its translocation in the ribosome. Cell. 2014; 157:823–831. [PubMed: 24792965]
66. Yang Z, et al. UCSF Chimera, MODELLER, and IMP: an integrated modeling system. Journal of structural biology. 2012; 179:269–278. [PubMed: 21963794]
67. The CCP4 suite: programs for protein crystallography. Acta Crystallogr D Biol Crystallogr. 1994; 50:760–763. [PubMed: 15299374]
68. Landau M, et al. ConSurf 2005: the projection of evolutionary conservation scores of residues on protein structures. Nucleic acids research. 2005; 33:W299–302. [PubMed: 15980475]
69. Holm L, Kaariainen S, Rosenstrom P, Schenkel A. Searching protein structure databases with DaliLite v.3. Bioinformatics. 2008; 24:2780–2781. [PubMed: 18818215]
70. Barton GJ. ALSCRIPT: a tool to format multiple sequence alignments. Protein engineering. 1993; 6:37–40. [PubMed: 8433969]
71. Hegemann B, et al. Systematic phosphorylation analysis of human mitotic protein complexes. Science signaling. 2011; 4:rs12. [PubMed: 22067460]
72. Kraft C, et al. Mitotic regulation of the human anaphase-promoting complex by phosphorylation. The EMBO journal. 2003; 22:6598–6609. [PubMed: 14657031]
73. Steen JA, et al. Different phosphorylation states of the anaphase promoting complex in response to antimitotic drugs: a quantitative proteomic analysis. Proceedings of the National Academy of Sciences of the United States of America. 2008; 105:6069–6074. [PubMed: 18420821]

Europe PMC Funders Author Manuscripts

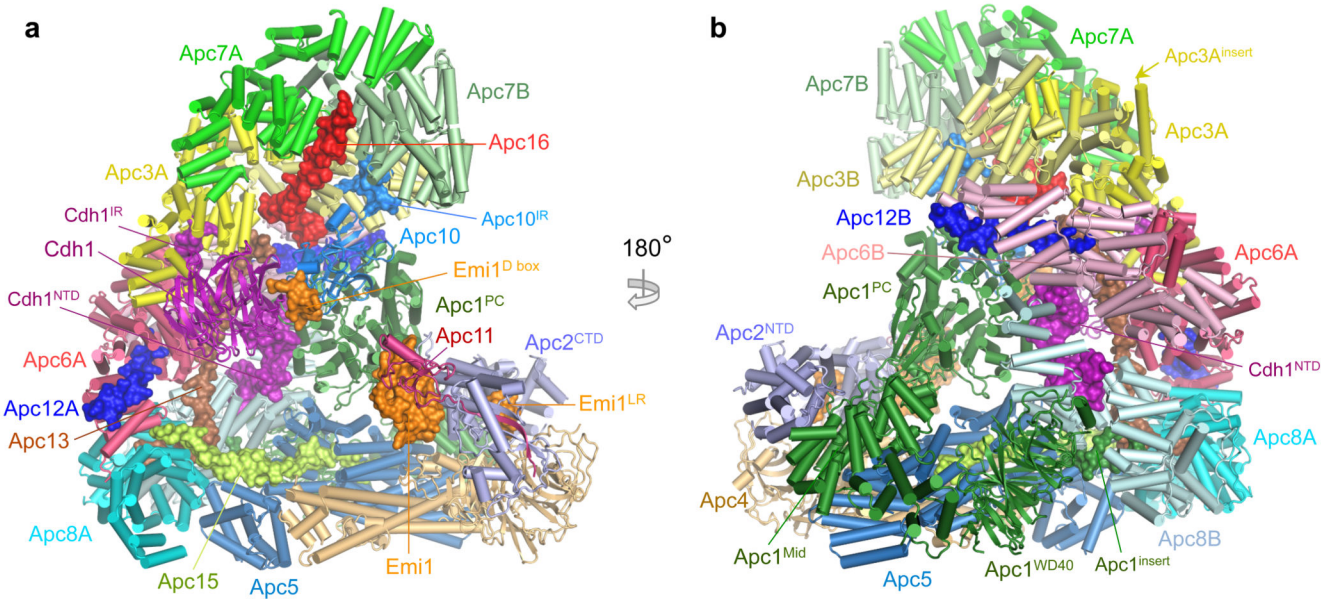

Figure 1. EM reconstructions of the APC/C$^{Cdh1.Emi1}$ complex

(**a,b**) Two views of the atomic structure of APC/C$^{Cdh1.Emi1}$. Large subunits are shown in cartoon, whereas the four small subunits, Emi1, Cdh1^{NTD}, Cdh1^{IR} and Apc10^{IR} are shown as surface representations. Emi1 interacts with the substrate-recognition and catalytic modules.

Europe PMC Funders Author Manuscripts

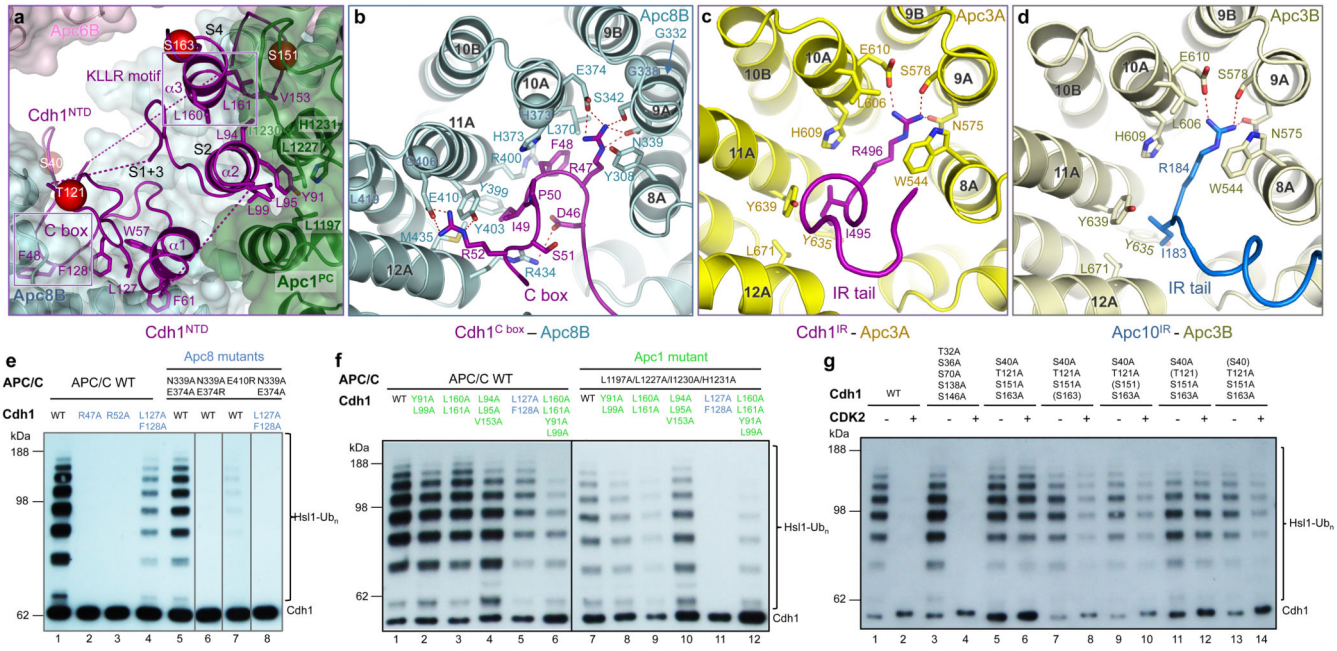

Figure 2. The C box of Cdh1 and IR tails of Cdh1 and Apc10 interact with structurally related sites on Apc8 and Apc3

(**a**) Cdh1^{NTD} binds to Apc8 and Apc1. Segments 1 and 3 of Cdh1^{NTD} including the C box interact with Apc8, whereas segments 2 and 4 interact with Apc1^{PC}. Segments 1-4 are labelled as S1-4. Phosphorylation sites S40, S151 and S163 as red spheres. (**b**) Details of the C box-interactions. The R47 and I49 interaction sites are structurally related to the IR tail-binding sites for Cdh1 and Apc10 in Apc3 shown in (**c, d**). *S. cerevisiae CDC23* (Apc8) temperature-sensitive mutations [23] map to the C box-binding site (Cα of mutant residues shown as spheres in (**b**)). (**e**) Mutation of C box-residues Arg47 and Arg52 eliminates APC/C^{Cdh1} activity, as do mutation of Apc8 residues that interact with either Arg47 or Arg52. (**f**) At the Cdh1^{NTD} – Apc1^{PC} interface multiple residues cooperate to mediate APC/C – Cdh1 interactions. (**g**) S40, S151 and S163 mediate the negative regulation of Cdh1 by CDK phosphorylation.

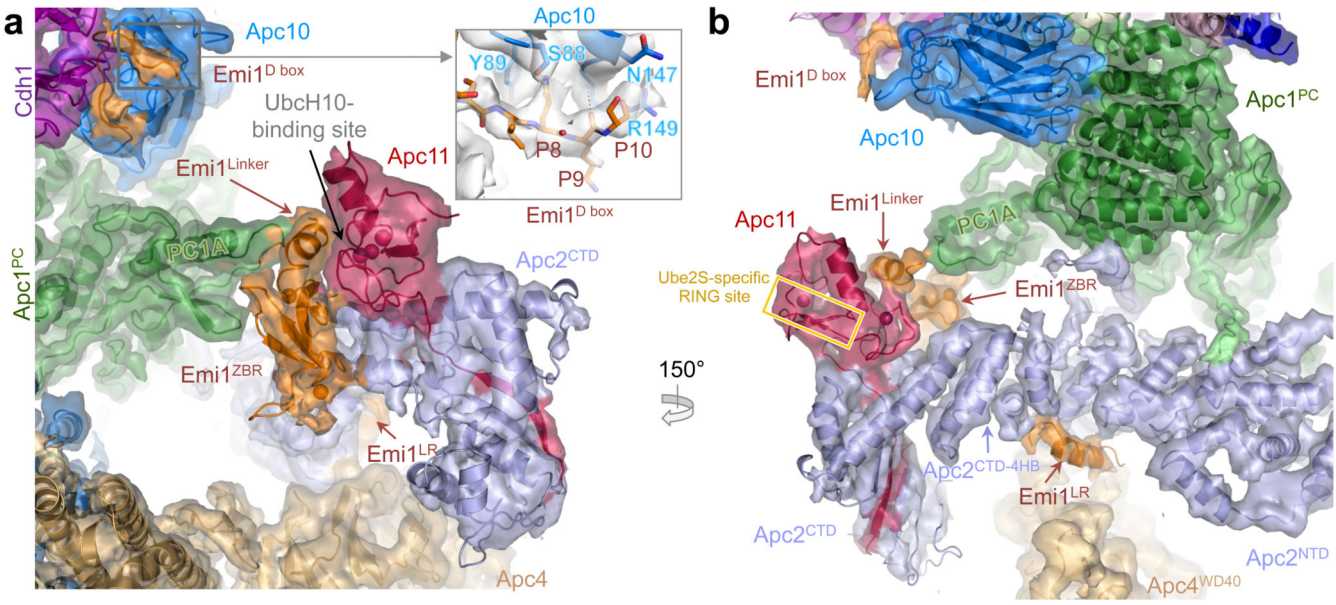

Figure 3. Interactions of Emi1 with Apc2^{CTD}-Apc11^{RING} and D box receptor of Cdh1 and Apc10

(**a**) and (**b**) views of the EM density and underlying secondary structure. Emi1 elements are shown: D box (Emi1$^{D\text{-}box}$); Emi1^{Linker} and Emi1^{ZBR} interconnects Apc1^{PC} with Apc2^{CTD} and Apc11^{RING}. Both Emi1^{Linker} and Emi1^{ZBR} block the UbcH10-binding site on Apc11, but not the Ube2S-specific site [26]. The C-terminal LRRL tail (Emi1^{LR}) of Emi1 binds to Apc2^{CTD}.

Europe PMC Funders Author Manuscripts

Europe PMC Funders Author Manuscripts

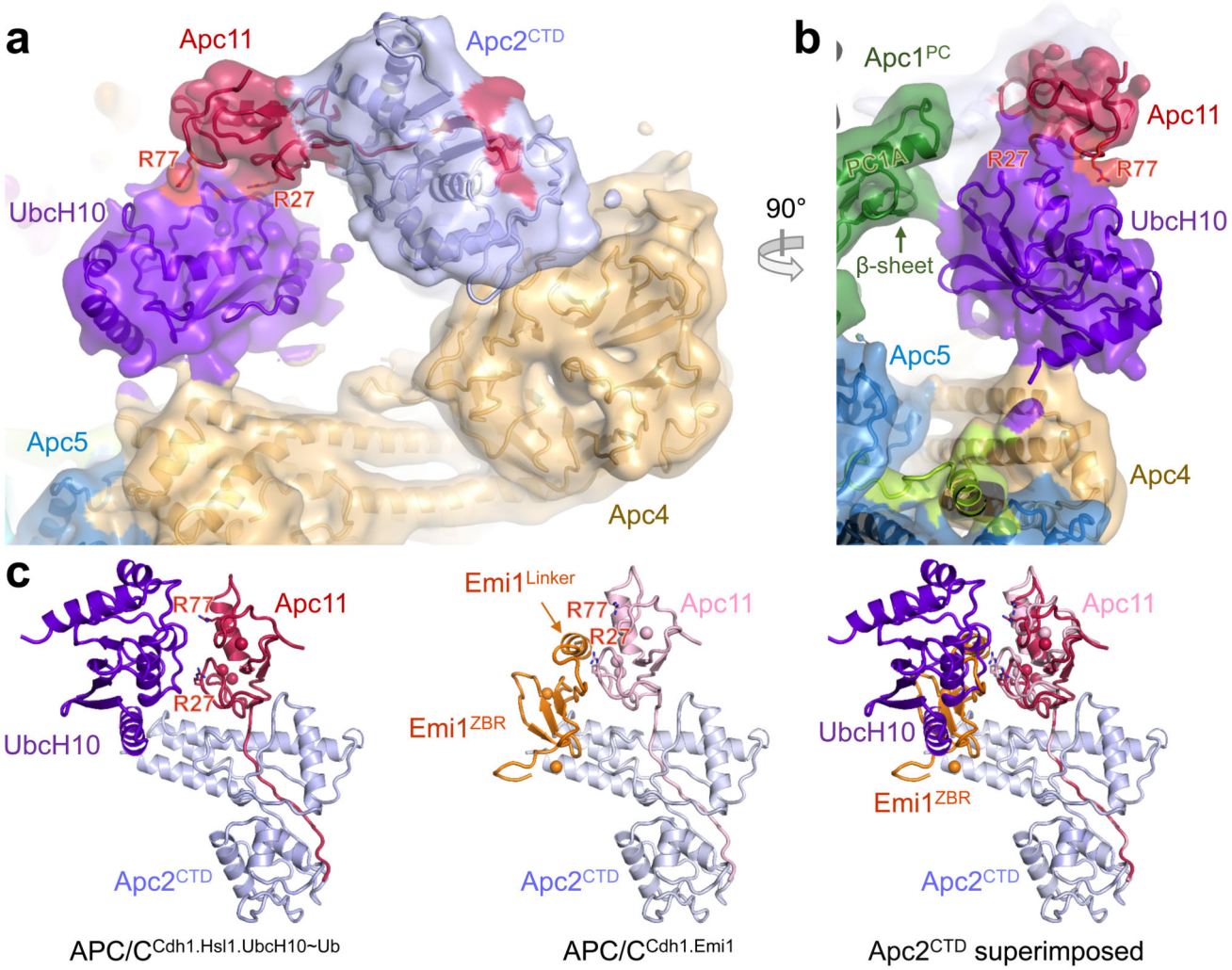

Figure 4. Structure of the APC/C$^{Cdh1.Hsl1.UbcH10\text{-}Ub}$ complex reveals the location of UbcH10

(**a**) and (**b**) views of the EM density at the catalytic centre with UbcH10-ubiquitin. No density for the ubiquitin moiety was recovered. R27 and R77 of Apc11, required for UbcH10 interactions [26] are indicated. (**c**) The UbcH10- and Emi1-binding sites of Apc11^{RING} overlap. The Apc11^{RING} orientation differs slightly in the two complexes.

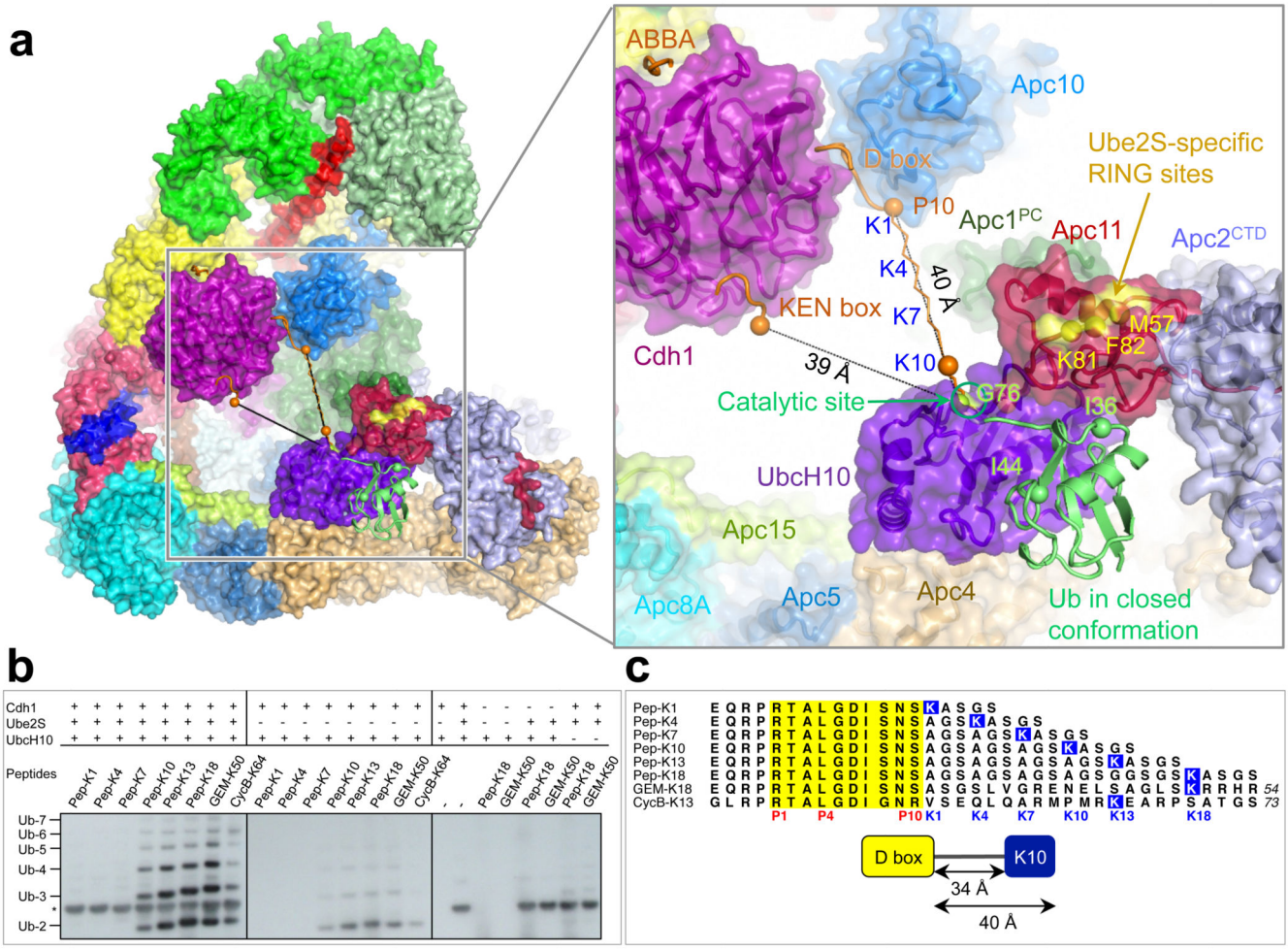

Figure 5. The relative position of the catalytic and substrate-recognition modules defines the target lysine

(**a**) View of APC/C$^{Cdh1.Hsl1.UbcH10\text{-}Ub}$ with close-up view of the catalytic and substrate-recognition modules. A UbcH10-ubiquitin conjugate is modelled in the closed conformation [29]. The Ube2S-specific site of Apc11^{RING} (for distal Ub positioning) [26] is indicated. KEN box and ABBA motif modelled on [39]. The distance from the D and KEN boxes to the catalytic centre of UbcH10 (measured as Cα-CO distance: P10 of D box and 'N' of KEN box to Gly76 of ubiquitin) is indicated. A ten-residue linker is modelled connected to P10 of the D box with Lys at K10. Spheres denote Cα-atoms of D box-P10 and linker-K10. (**b**) The reactivity of defined peptides with progressively longer spacers separating the D box and accepter lysine residue (sequences shown in (**c**)). Only peptides with a lysine ten or more residues C-terminal to the D box are substrates. *: Ube2S-specific band. (**c**) Peptide sequences used in ubiquitination assays. D box in yellow, target lysines in blue.

Europe PMC Funders Author Manuscripts